This is the peer-reviewed, final accepted version for American Mineralogist, published by the Mineralogical Society of America.
The published version is subject to change. Cite as Authors (Year) Title. American Mineralogist, in press.
DOI: https://doi.org/10.2138/am-2020-7014. http://www.minsocam.org/

REVISION 2

Word Count: 11442 words

Experimental evaluation of a new H_2O-independent thermometer based on olivine-melt Ni partitioning at crustal pressure

Xiaofei Pu[1]*, Gordon M. Moore[2], Rebecca A. Lange[1], Jack P. Touran[2], Joel E. Gagnon[3]
1.University of Michigan, Ann Arbor, MI, 48109, USA
2. NASA Johnson Space Center, Houston, TX, 77058, USA.
3. University of Windsor, Windsor, ON, N9B 3P4, Canada
Corresponding Author Email: pux@umich.edu

Abstract

An olivine-melt thermometer based on the partitioning of Ni ($D_{Ni}^{ol/liq}$) was hypothesized by Pu et al. (2017) to have a negligible dependence on dissolved water in the melt (and pressure variations from 0-1 GPa), in marked contrast to thermometers based on $D_{Mg}^{ol/liq}$. In this study, 15 olivine-melt equilibrium experiments were conducted on a basaltic glass starting material (9.6 wt% MgO; 353 ppm Ni) to test this hypothesis by comparing the effect of dissolved H_2O in the melt on $D_{Mg}^{ol/liq}$ and $D_{Ni}^{ol/liq}$ on the same set of experiments. Results are presented for six anhydrous experiments at 1 bar, two anhydrous experiments at 0.5 GPa, and seven hydrous experiments at 0.5 GPa. Analyzed olivine and glass compositions in the quenched run products were used to calculate $D_{Mg}^{ol/liq}$ and $D_{Ni}^{ol/liq}$ values for each experiment, which in turn permit temperature to be calculated with the Mg- and Ni-thermometers calibrated in Pu et al. (2017) on anhydrous, 1-bar experiments from the literature. The Ni-thermometer recovers the temperatures of all fifteen experiments from this study with an average deviation of -3 °C, including those with up to 4.3 wt% H_2O dissolved in the melt. In contrast, the Mg-thermometer recovers the anhydrous, 1-bar experimental temperatures within +14 °C on average, but overestimates the hydrous experimental temperatures by +49 to +127˚C, with an average of +83˚C. When the Mg-thermometer of Putirka et al. (2007) is applied, which includes a correction for analyzed H_2O (≤4.3 wt%) in the quenched melts of the run products, all

experimental temperatures are recovered with an average (±1σ) deviation of +7 °C. The combined results show that $D_{Ni}^{ol/liq}$ has a negligible dependence on dissolved water in the melt (≤ 4.3 wt% H_2O), which is in marked contrast to the strong dependence of $D_{Mg}^{ol/liq}$ on water in the melt. An understanding of why $D_{Ni}^{ol/liq}$ is insensitive to dissolved water, unlike $D_{Mg}^{ol/liq}$, is obtained from spectroscopic evidence in the literature, which shows that Ni^{2+} (transition metal) and Mg^{2+} (alkaline earth metal) have distinctly different average coordination numbers (predominantly 4-fold and 6-fold, respectively) in silicate melts and that 4-fold coordinated Ni^{2+} is unaffected by the presence of dissolved water in the melt. This difference in coordination number explains why $D_{Ni}^{ol/liq}$ and $D_{Mg}^{ol/liq}$ each have a different dependence on pressure, anhydrous melt composition, and melt water content. Application of the Ni-thermometer of Pu et al. (2017) to five natural samples from the Mexican arc, for which H_2O contents (3.6-6.7 wt%) in olivine-hosted melt inclusions are reported in the literature, leads to temperatures that match those obtained from the Putirka et al. (2007) Mg-thermometer that corrects for analyzed H_2O contents. This study demonstrates that a thermometer based on $D_{Ni}^{ol/liq}$ can be applied to hydrous basalts at crustal depths without the need to correct for dissolved water content or pressure.

INTRODUCTION

Knowledge of the magmatic temperature of arc basalts is key to understanding subduction zone processes, including the interplay between hydrous flux melting and decompressional melting. Geodynamic models of these processes rely on high-quality data on both the temperature and water contents of erupted arc basalts. Most published olivine-melt thermometers are based on the partitioning of Mg (defined here as $D_{Mg}^{ol/liq} = X_{MgO}^{ol} / X_{MgO}^{liq}$) (e.g. Beattie, 1993; Herzburg and O'Hara, 2002), which has a strong dependence on dissolved water in the melt (e.g. Putirka et al., 2007). Therefore, olivine-melt Mg-thermometers require a correction term based on melt H_2O content (Putirka et al., 2007; Putirka, 2008). A priori

This is the peer-reviewed, final accepted version for American Mineralogist, published by the Mineralogical Society of America.
The published version is subject to change. Cite as Authors (Year) Title. American Mineralogist, in press.
DOI: https://doi.org/10.2138/am-2020-7014. http://www.minsocam.org/

knowledge of the H_2O content in the melt at the time of olivine crystallization is therefore required for high-quality temperature estimates, yet it is not always available.

To address this issue, Pu et al. (2017) proposed an olivine-melt thermometer based on the partitioning of Ni, which is largely independent of dissolved H_2O in the melt. In that study, a new olivine-melt Ni-thermometer was calibrated on a dataset of 123 anhydrous, 1-bar olivine-melt experiments from 16 studies in the literature. This 1-bar data set spans a wide range of temperatures (1170-1650°C), olivine composition (Fo_{36-100}; 0.10-15.7 wt% NiO), and liquid composition (37-66 wt% SiO_2, 4-40 wt% MgO, 0-31 wt% FeO^T, 0-29 wt% CaO, 0-22 wt% Al_2O_3, 0-12 wt% Na_2O, 0-11 wt% K_2O, 0-3 wt% MnO and 0-1.7 wt% P_2O_5, 107-11087 ppm Ni). A similar olivine-melt Mg-thermometer was calibrated on the same data set. Pu et al. (2017) employed the Beattie (1993) model equation for both thermometers, but used mole fractions instead of cation fractions:

$$lnD_i^{ol/liq} = a + \frac{b}{T} + c\left(lnX_{NM}^{liq}\right) + d\left(lnX_{SiO2}^{liq}\right) + e\ (NF) \qquad (1)$$

In Equation 1, T is in Kelvin, $X_{NM}^{liq} = X_{FeO}^{liq} + X_{MgO}^{liq} + X_{MnO}^{liq} + X_{CaO}^{liq} + X_{CoO}^{liq} + X_{NiO}^{liq}$, (mole fraction components), $X_{SiO2}^{liq}$is the mole fraction of SiO_2 in the melt, and NF = 3.5 x ln(1-X_{Al2O3}) + 7 x ln(1-X_{TiO2}). The fitted parameters for i = Mg or Ni are reported in Table 1.

Pu et al. (2017) applied the two thermometers to a set of mid-ocean ridge basalts (MORB; Allan et al., 1989) and a set of subduction-zone basalts and basaltic andesites from the Mexican volcanic arc (Ownby et al., 2011). The average difference between the Mg- and Ni-thermometers (T_{Mg} - T_{Ni}) is -3˚C for a set of MORB samples, which are close to anhydrous (estimated at ~0.1 wt% H_2O for MORBs with <0.07 wt% K_2O; Langmuir et al., 2006) and +112˚C for the hydrous arc samples, for which there are analyses of ≤3.9-5.7 wt% H_2O in olivine-hosted melt inclusions (Johnson et al., 2008, 2009). Because the Mg- and Ni-thermometers were calibrated on an identical set of experiments, the systematic difference between the results of the two thermometers when applied to subduction-zone basalts cannot be attributed to

differences in their respective calibrations. Note also that the compositions of both the MORBs and the arc samples fall within the range of the liquids in the calibration dataset. As a consequence, Pu et al. (2017) attributed the large differences in calculated temperatures (T_{Mg}-T_{Ni}) to the difference in sensitivity of $D_{Mg}^{ol/liq}$ and $D_{Ni}^{ol/liq}$ to dissolved H_2O in the arc basaltic melts.

Outside of three hydrous experiments on a basaltic andesite from Moore and Carmichael (1998), for which the Ni content in the quenched melt in each run product was analyzed and reported in Pu et al. (2017), there are no hydrous olivine-melt equilibrium experiments available in the literature where the Ni contents in coexisting olivine and melt are reported. In this study, we present a set of new olivine-melt Ni partitioning experiments on a basaltic starting composition, at 1-bar and 0.5 GPa with variable amounts of dissolved water, with the following three goals: 1) to further evaluate if there is any resolvable dependence of melt H_2O content on olivine-melt Ni partitioning; 2) to test the 1-bar Ni-thermometer under both hydrous and anhydrous conditions at 0.5 GPa; and 3) to compare the relative performance of the 1-bar, anhydrous Mg-thermometer and Ni- thermometer on olivine-melt equilibrium experiments with and without the presence of H_2O in the melt. Additionally, the performance of the Ni-thermometer was compared to the Mg-thermometer of Putirka et al. (2007), which includes a correction for dissolved H_2O in the melt.

Another objective of this study is to apply the Mg- and Ni-thermometers to high-MgO lavas erupted in the Mexican arc, for which analyses of H_2O in olivine-hosted melt inclusions have been reported in the literature. Pu et al. (2017) previously did this for three calc-alkaline basalts erupted from the Michoacán-Guanajuato segment of the Mexican subduction zone, for which olivine-hosted melt inclusions were analyzed for H_2O (Johnson et al., 2008; 2009). In this study, two additional samples from the Mexican arc are examined, namely K-rich basanites from two cinder cones (Apaxtepec and La Erita) adjacent to Volcán Colima. H_2O contents of up to 6.2 and 6.7 wt% were reported based on FTIR measurements of olivine-hosted melt inclusions in scoria samples from these two cones by Vigouroux et al. (2008) and Maria and Luhr (2008),

respectively. In this study, the goal is to compare temperatures calculated with the Ni-thermometer of Pu et al. (2017) without any H_2O correction to those calculated with the Mg-thermometer of Putirka et al. (2007), which includes a correction for the H_2O contents analyzed in the melt inclusions. This comparison provides a test of whether or not the Ni-thermometer requires a correction for H_2O when applied to hydrous arc basalts.

EXPERIMENTAL METHODS

Synthesis of starting material

The starting material for all experiments in this study is a calc-alkaline basalt sample from the Mexican arc (UR-46, Ownby et al., 2011; Pu et al., 2017), with 52 wt% SiO_2, 9.4 wt% MgO and 231 ppm Ni (Table 2). Pieces of the natural sample were crushed in a tungsten-carbide shatter box into a fine powder. Reagent grade NiO powder was mixed with the natural rock powder in a ceramic mortar and pestle, in order to increase the Ni content of the starting material (~350 ppm) for all experiments, but kept to levels that do not significantly exceed those found in natural arc basalts. The mixed powder was placed in a platinum crucible and heated in air to 1450°C for two hours. The sample was then quenched in deionized water at room temperature, producing a crystal-free glass (Table 2).

One-bar olivine-melt equilibrium experiments

Experimental setup

One-bar experiments were conducted in a vertical Deltech furnace with the oxygen fugacity (f_{O2}) controlled by a mixture of CO-CO_2 gases. A brief outline of the experimental setup is presented here, with detailed description provided in Appendix A. Temperature was monitored by an S-type thermocouple (± 3°C), calibrated against the melting temperature of gold (± 1°C) and placed at the hot spot of the furnace; the combined uncertainty in temperature

is ± 4°C. Oxygen fugacity was monitored with an yttria-stabilized zirconia oxygen sensor located adjacent to the thermocouple and samples.

The starting glass was crushed to a powder and mixed with a poly-vinyl alcohol (PVA) solution to make a paste, which was then placed on two separate $Au_{60}Pd_{40}$ wire loops (for duplication purposes) that were hung from a Pt wire cage. During quench, the Pt cage was dropped into a cup of cold, distilled water at the base of the furnace. The experimental run products consisted of glass beads attached to the $Au_{60}Pd_{40}$ wire loops. The glass beads were readily removed and multiple glass chips from each experiment were embedded in epoxy grain mounts for compositional analyses. All $Au_{60}Pd_{40}$ wire used in the experiments was first pre-saturated to minimize loss of Fe and Ni to the wire loop. Pre-saturation runs were conducted under identical conditions (temperature, f_{O2}, duration) as the final experimental runs.

One-bar liquidus temperature and comparison with MELTS

According to MELTS (Ghiorso and Sack, 1995; Asimow and Ghiorso, 1998), the 1-bar olivine liquidus temperature for UR-46 basalt (Table 2) along the Ni-NiO oxygen fugacity buffer (NNO) is 1254°C, and plagioclase joins olivine at 1205°C under equilibrium crystallization conditions. To check for consistency between MELTS and this experimental study, two 1-bar crystallization experiments at NNO were conducted to constrain the temperature of the olivine liquidus. The starting glass material was taken to 1250 and 1240°C, held for 24 hours in each case, and then quenched.

Two temperature-path trajectories

Six olivine-melt Mg- and Ni-partitioning experiments were performed at 1-bar at temperatures designed to be ≤50 °C below the olivine liquidus. All experiments started with a crystal-free glass, but two temperature-path trajectories were undertaken (Table 3; Fig. 1) with the difference that the final experimental temperature was reached from lower vs. higher

159 temperatures. In the "bottom-up" experiments, the sample briefly transits through the
160 supercooled liquid region between the glass transition temperature and final equilibration
161 temperature, where a relatively large undercooling ($\Delta T = T_{liquidus} - T_{supercooled\ liquid}$) leads to high
162 nucleation rates and low crystal growth rates (Fig. 1). Thus, when the supercooled liquid
163 reaches the final equilibration temperature, it may contain some nuclei, which minimizes a
164 kinetic delay to nucleation. Experiments run in this manner have been shown to reach mineral-
165 melt compositional equilibrium in relatively viscous melts (e.g. rhyolite). For example, Waters
166 and Lange (2017) showed that in hydrous rhyolite melts with a viscosity of ~10^{4-5} Pa-s,
167 orthopyroxene-liquid closely approached Fe-Mg exchange equilibrium within <24 hours. For the
168 1-bar experiments in this study, the anhydrous basalt liquids have a lower melt viscosity (~10^3
169 Pa-s; Table 3), and are therefore expected to reach mineral-melt compositional equilibrium with
170 less than 24 hours.
171 Three 1-bar experiments from this study were conducted with the "bottom-up" trajectory.
172 In two cases, the starting glass was quickly brought up to a final run temperature of 1225 °C
173 (with an fO_2 equivalent to Ni-NiO (NNO) buffer) and then held for 12 and 24 hours, respectively,
174 prior to quench. The purpose of the two dwell times is to check for any change in olivine and
175 melt compositions, reflecting an approach to equilibrium. A third experiment was also held for
176 24 hours at 1225 °C, but at an fO_2 that is two log units above NNO; the results from that run
177 product permit an evaluation of whether the partitioning behavior of Ni^{2+} and Mg^{2+} is affected by
178 a change in the melt ferric-ferrous ratio.
179 For the other three 1-bar experiments, the "top-down" temperature path was employed,
180 where the starting glass was first taken to 1275 °C (above olivine liquidus temperature) and held
181 for two hours (ΔNNO = 0) to eliminate any nuclei that may have formed during heating of the
182 glass up to super-liquidus conditions. After the two-hour dwell, temperature was abruptly
183 dropped to the final equilibration temperature (1225 or 1200°C; f_{O2} adjusted to keep sample at

NNO) within 5 minutes, and held for durations that ranged from 8-24 hours prior to quench. The magnitude of the undercooling was designed to be ≤50°C.

The primary purpose in performing experiments with a "top-down" trajectory is to approximate conditions that may occur in nature, where hydrous, fluid-undersaturated, arc basaltic liquids segregate from the mantle and ascend rapidly along fractures, reaching super-liquidus conditions as the liquidus temperature drops with decreasing pressure. During ascent, eventually fluid saturation will occur, and the loss of an H_2O-rich fluid will cause the liquidus temperature to increase with decreasing pressure; therefore, the hydrous basalt will eventually cross its liquidus during ascent, but from a super-liquidus condition with no pre-existing nuclei. There will be an initial kinetic delay in crystal nucleation, which promotes the development of an effective undercooling (ΔT_{eff}) (e.g. Hammer and Rutherford, 2002) that corresponds to high crystal growth rates and low nucleation rates (Fig. 1) and enables the growth of large, sparse crystals (e.g. Lofgren et al., 1974). This ascent path and olivine crystallization history is supported by evidence from the compositions and textures of olivine phenocrysts in a set of calc-alkaline basalts from the Mexican arc (Pu et al., 2017). The outstanding question, however, is whether a kinetic delay in nucleation, followed by rapid phenocryst growth, leads to olivine compositions that deviate from equilibrium. Therefore, tests of olivine-melt disequilibrium were carried out in the experiments conducted with the "top-down" and "bottom-up" temperature trajectories in this study.

Piston-cylinder experiments

Experimental design

Experiments under both anhydrous and hydrous conditions at 0.5 GPa were conducted in a piston-cylinder apparatus (PC) at the University of Michigan Experimental Petrology Laboratory. A 19mm (3/4 inch) PC assembly was used to accommodate the lower pressure range of 0.5 GPa. The construction of the assembly (Appendix A) closely follows that described

in Moore et al. (2008), except our assembly is inverted (upside down) because of the different configuration between the end-loaded Rockland press at the University of Michigan Experimental Petrology Laboratory and the non-end-loaded QUICKpress manufactured by Depths of the Earth Co., which was used in Moore et al. (2008) at Arizona State University. Details of the determination of the hotspot, thermal gradient, temperature uncertainty (± 8 °C) and experimental procedure are presented in Appendix A, and they broadly follow protocols presented in Tenner et al. (2007).

The primary goal of the PC experiments is to evaluate if $D_{Ni}^{ol/liq}$ is dependent on water content in the melt, and thus test the accuracy of the Ni-thermometer of Pu et al. (2017) under hydrous conditions. The objective is to reproduce conditions broadly relevant to natural hydrous basalts undergoing olivine crystallization from a 100% liquid over a relatively short time interval (i.e., 1 day or less) and to evaluate evidence for olivine-melt disequilibrium in the run products. For a subset of experimental run products, the measurement of Fe^{3+}/Fe^{T} ratio in the quenched glass phase allows calculation of $^{Fe2+-Mg}K_D$ (olivine-liq) = $(X_{FeO}/X_{MgO})^{ol}/(X_{FeO}/X_{MgO})^{liq}$), which can be used to test for disequilibrium. In some cases, experimental condition and trajectory were identical except for different dwell times; in other cases, the runs were exactly replicated as a check of reproducibility.

The PC experiments in this study were designed to minimize Ni and Fe loss from the basalt sample to the enclosing capsule material by pre-saturating $Au_{75}Pd_{25}$ capsules prior to all experiments. To pre-saturate, each capsule was welded on one end in trash-can style (with a rimmed flat-bottomed lid on a cylindrical trash can), filled with the starting glass powder, and then a flat lid was placed on top, but not welded. This capsule assembly was heated in the 1-bar Deltech furnace for the same amount of time as the total experimental time in PC at an oxygen fugacity one log unit below the Ni-NiO buffer, at 1250˚C. After each pre-saturation experiment, the assembly was air quenched. The complete removal of the glass inside the capsule was achieved by gentle pressing on the capsule wall with tweezers to break off the

larger chunks, followed by soaking the pre-saturated capsule in hydrofluoric acid at room temperature for 6-10 hours.

For the two anhydrous PC experiments, the pre-saturated capsules were loaded with starting glass chips to reduce absorption of moisture from the air into the powder, before the lid was welded shut. For the hydrous PC experiments, deionized water was first added to the pre-saturated capsule with a micro-syringe, followed by the powdered glass starting material. The capsules were weighed after each step of loading, as well as before and after the PC experiment. The loss of mass (mostly H_2O) during welding was within 0.3mg (<0.5 wt% error for the added H_2O). The weight of all water-bearing capsules was monitored before and after 10-30 minutes in a drying oven at 120˚C, to confirm the final seal on the capsule. The amount of water added was designed to achieve ~5 wt% H_2O in the basalt melt; higher water contents were avoided to minimize the presence of quench crystals in the experimental run product. As a result, the experiments were H_2O-undersaturated, and therefore some H_2O loss during the experimental runs was expected, either through diffusion of H_2 and/or H_2O across the capsule wall (e.g. Hall et al., 2004; Patiño Douce and Beard, 1994). Therefore, a key objective of this study was to evaluate if a change in melt H_2O content (a common scenario during degassing-induced crystallization in nature) has any effect on the partitioning of Ni between olivine and melt.

Two temperature-path trajectories

The same two trajectories used in the 1-bar experiments were also applied to the PC experiments (Table 3). For the two nominally anhydrous experiments (PC-33 and PC-35; Table 3), the “bottom-up” path was followed, where the starting glass was taken up to the final temperature and held for 48 and 29.5 hours at 1192°C (note, this temperature is below the expected plagioclase-in curve at 0.5 GPa on the basis of MELTS calculations). The “bottom-up” path was also followed for two hydrous experiments (PC-10 and PC-12; Table 3), where the

262 samples were taken directly up to their respective final equilibration temperatures (1137 and
263 1127 °C) and held for 12 hours. The remaining five hydrous experiments (Table 3) were all
264 conducted with the "top-down" trajectory, where the samples were first taken up to temperatures
265 above their liquidus and held for 1 to 4 hours, and then the temperature was rapidly dropped to
266 their respective final equilibration temperatures (1127, 1112 or 1102 °C) and held for 8 to 12
267 hours.
268
269 *Quench and preparation of samples for analyses*
270 At the end of each PC experiment, an isobaric quench was achieved by shutting off the
271 power supply while maintaining the pressure using a hydraulic oil pump. During the quench, the
272 thermocouple recorded temperatures below 600˚C after 5 seconds, and below 300˚C after 10
273 seconds. After the quench, the capsule was retrieved and checked for any signs of melting or
274 leakage by examination under a stereoscope. The quenched capsule was then soaked
275 overnight in hydrofluoric acid to remove any Pyrex® powder around the capsule derived from
276 the PC assemblage. The capsule was then weighed to check for any change before and after
277 the experiment, after which the entire capsule was mounted in epoxy and double polished into a
278 200-300μm thick plate for subsequent analyses.
279
280 **ANALYTICAL METHODS**
281 *Whole-rock analyses of two natural samples*
282 The two natural K-rich basanite samples (COL-1001B; COL-1015) from the Mexican arc
283 examined in this study are from Carmichael et al. (2006). In this study, new sample powders
284 were obtained from the same rock pieces from which thin sections were cut. The sample
285 powders were analyzed for major and trace elements by inductively coupled plasma-mass
286 spectrometry (ICP-MS) at Activation Laboratories of Ancaster, Ontario, Canada.
287

Electron microprobe analysis (EMPA)

Compositional analyses of experimental glass, olivine, plagioclase, and the AuPd capsule material were conducted with a five-spectrometer Cameca SX-100 electron microprobe at the University of Michigan Electron Micro-Analysis Laboratory (EMAL). Olivine crystals were analyzed under a focused beam, with an acceleration voltage of 15kV and a beam current of 20nA. Eight elements were measured (Mg, Al, Si, Ca, Mn, Fe, Cr, Ni) with peak counting time of 30s for each element. Oxygen was calculated by cation stoichiometry, which was then used as input into the Cameca PAP correction program. The standards used for olivine microprobe analyses are the same as those described in Pu et al. (2017). A second standard (Bolton Forsterite; $Fo_{98.5}$) was used as an additional check of the olivine analyses. For the two natural samples, analytical traverses across 20-30 different olivine crystals were conducted. Analyses were conducted every 20-30 microns during these traverses, leading to approximately 400-600 olivine analyses for each sample. In the experimental run products, in cases where the olivine crystals are larger than 20μm in size, more than one analysis was conducted per crystal, with an effort to analyze areas both near and far from the rim. For smaller crystals, only one analysis per grain was possible.

Glass in the experimental run products was analyzed with an acceleration voltage of 15 kV, a beam current of 10 nA and the beam was defocused to 10μm. Ten elements were measured (Na, Mg, Al, Si, P, K, Ca, Ti, Fe, Mn), with peak counting times of 10s for Na, Al, Si, and K and 20s for the rest of the elements. For a subset of samples, the Ni content of the glass was also analyzed with 60s of counting time on two spectrometers. The standards used for the glass analyses are shown in Appendix B. A second standard (NHNM-113716-1; Smithsonian Indian Ocean Basaltic Glass) was used to evaluate the quality of the basalt glass analyses. Glass was analyzed in areas both adjacent to and relatively far from olivine crystals in each experimental run product to test disequilibrium.

313 AuPd capsules from six PC experiments were analyzed with 20kV acceleration voltage,
314 30μm beam current and focused beam for four elements: Au, Pd, Fe and Ni. Pure metal
315 standards were used as calibration standards for each element. The counting time was 30s for
316 each element, with Fe and Ni measured on two spectrometers due to their lower concentration
317 in the alloy. The goal of this measurement is to apply the AuPdFe oxybarometer calibrated by
318 Barr and Grove (2010) to evaluate the fO_2 recorded in the sample capsule at the time of
319 quench, as well as monitoring Fe and Ni contents in the capsule material.
320
321 *Laser-ablation inductively-coupled plasma mass spectrometry (LA-ICP-MS)*
322 The concentration of Ni in the starting glass material and in all experimental glasses was
323 analyzed by laser ablation inductively-coupled plasma mass spectrometry (LA-ICP-MS) in the
324 Element and Heavy Isotope Analytical Laboratories (EHIAL) at the University of Windsor. The
325 instrumentation includes a PhotonMachines Analyte Excite 193nm, short-pulse-width (< 4 ns),
326 Ar-F excimer laser ablation system coupled with an Agilent 7900, fast-scanning quadrupole ICP-
327 MS. For each LA-ICP-MS analysis, 30s of background (gas and instrument) counts with the
328 laser off, and 40s of ablation signal counts with the laser on were acquired. A 50μm spot size
329 was used for all glass analyses.
330 The NIST 610 synthetic glass standard reference material was analyzed every 40 to 60
331 min during the analytical session and was used as the external calibration standard and to
332 correct for instrumental drift. Four isotopes, ^{25}Mg, ^{27}Al, ^{43}Ca, ^{44}Ca, were used as internal
333 calibration standards to correct for differences in the rate of ablation between the external
334 calibration standard (NIST 610) and the samples. The concentrations of the internal standards
335 were obtained from microprobe analyses on the samples. Concentrations of Ni were
336 determined using signal intensities obtained on masses ^{60}Ni and ^{62}Ni. For each spot analysis,
337 the reported Ni concentration is the average of the eight values calculated for ^{60}Ni and ^{62}Ni
338 using the four internal standard isotopes and corrected from ablation yield relative to NIST 610.

Data processing was conducted using the software package SILLS (Guillong et al., 2008), which accounts for instrumental drift over time. The trace element concentrations of NIST 610 were adopted from the recommended average values in Pearce et al. (1997). The analytical uncertainties for both ^{60}Ni and ^{62}Ni analyses are 5% (1σ) for all glass analyses.

Fourier-transform infrared spectroscopy (FTIR)

For all the high-pressure experiments in this study, the quenched glasses in the run products were analyzed for H_2O concentration with a Perkin-Elmer GX Fourier transform infrared spectrometer (FTIR) at the University of Michigan. A mid-IR source and KBr beam splitter was used, with the aperture size of 100x100μm. Samples were mounted in epoxy and polished on both sides down to a thickness of 200-400μm. For each FTIR spectrum, the baseline was fit with a flexi curve, similar to that described in Zhang et al. (1997). The molar absorptivity is 0.67 (L•cm/mol) for the 5200cm^{-1} band of molecular H_2O and 0.62 (L•cm/mol) for the 4500 cm^{-1} band of hydroxyl group (OH), following Dixon et al. (1995). The total H_2O content was determined by the summation of molecular H_2O and hydroxyl group (OH) concentration in the melt. The density of the hydrous glass was calculated from Lange and Carmichael (1990), Lange (1997) and Ochs and Lange (1999). A second-order iteration was applied so that the final calculation of H_2O content, which depends on glass density, matched the value calculated based on Beer-Lambert Law for the FTIR spectrum. For the nominally anhydrous experiment conducted in the piston-cylinder apparatus, analysis of the quenched glass used the 3550cm^{-1} band of total molecular H_2O with a molar absorptivity of 63 (L•cm/mol), following Dixon et al. (1995).

Micro-XANES spectroscopy measurements of Fe^{3+}/Fe^{T} in quenched PC glasses

The Fe^{3+}/Fe^{T} ratio of the glass in three PC experiments (PC10, PC14, PC33) were analyzed by micro X-ray Absorption Near Edge Structure (μ-XANES) spectroscopy at station

13-ID-E in the Advanced Photon Source (APS), Argonne National Laboratory, USA. The measurements followed the methodology of Cottrell et al. (2009), with modifications from Cottrell et al. (2018) to mitigate oxidative beam damage in hydrous glass caused by high photon flux density, including decreasing the nominal flux to ~$1.5x10^9$ photons/second and defocusing the beam to 25x25μm. Flux density at the sample surface for these analyses was on the order of $2.4x10^6$ ph/sec/μm^2. Two spectra were collected for PC14 and one spectrum each were collected for PC10 and PC33. The $Fe^{3+}/\Sigma Fe$ ratios of unknown samples were determined through calibration of the area-weighted centroid energy of the pre-edge doublet of a suite of basaltic reference glasses against $Fe^{3+}/\Sigma Fe$ ratios determined independently by Mössbauer spectroscopy, corrected for the effects of recoil-free fraction on the Mössbauer spectra (Zhang et al., 2018). Basaltic reference glass LW_0 was used to monitor instrumental drift, and centroids were normalized to LW_0 ≡ 7112.3 eV. The root mean square uncertainty on glass Fe^{3+}/Fe^T ratio is ±0.01, predicted for the basalt calibration by Zhang et al. (2018).

RESULTS

Composition of experimental starting glass

Electron microprobe analyses of four glass chips synthesized at 1-bar in air confirm chemical homogeneity among all major elements for UR46Ni, with no Fe or alkali loss (Table 2, Appendix C). Back-scattered electron images confirm that the glass is free of crystals. Laser ablation ICP-MS analyses of 16 spots on four separate glass chips yield an average (± 1σ) Ni content of 353 (± 19) ppm (Table 2, Appendix C). The small standard deviation is within the analytical error (5% relative), which indicates the Ni content is homogenous in the starting material glass.

Location of 1-bar olivine liquidus temperature

The location of the 1-bar liquidus at NNO was experimentally determined to be between 1250 and 1240 °C. Samples held for 24 hours at 1250°C contained 100% glass with identical composition as the starting materials, whereas those held for the same duration at 1240°C contained <3% olivine crystals (Fo89.8± 0.2; Table 2, Appendix C). These results are in close agreement with liquidus determinations of 1251 and 1255°C, respectively, from the models of Beattie (1993) and Putirka et al. (2007), as well as the liquidus temperature of 1254°C obtained from MELTS (Ghiorso and Sack, 1995; Asimow and Ghiorso, 1998) for the starting composition at NNO.

The FeO and Fe_2O_3 concentrations in the experimental liquid at 1240°C and NNO were calculated from the model in Kress and Carmichael (1991), because it is what is used in MELTS. When combined with the analyzed olivine composition (Fo89.8), the resulting experimental $^{Fe2+-Mg}K_D$ (olivine-liq) value is 0.35 ± 0.02. These results match those calculated by MELTS, namely a liquidus olivine composition of Fo89 and a $^{Fe2+-Mg}K_D$ value of 0.35.

Run products from olivine-melt partitioning experiments

Crystal textures in "bottom-up" vs. "top-down" experiments

The run conditions and products of the six 1-bar and nine PC experiments are reported in Table 3. The "bottom-up" and "top-down" 1-bar experiments produced olivine crystals that are notably different in their size and textures. For the "bottom-up" experiments, in which the starting material transited through a supercooled liquid region characterized by high nucleation rates (Fig. 1) before arriving at the final equilibration temperature, the olivine crystals are euhedral and relatively small (≤ 30 μm; Fig. 2a). In contrast, the "top-down" experiments were taken directly to the final experimental temperature from a super-liquidus condition. A kinetic delay to nucleation produced an undercooling at the final equilibration temperature that corresponds to a region of relatively high crystal growth rate and low nucleation rate, which allowed the growth of large, sparse olivine crystals (Fig. 2b) that display diffusion-limited rapid

growth textures (e.g. dendritic ladder and hopper textures; Faura and Schiano, 2005; Ni et al., 2014). A similar contrast in crystal size and texture of olivine crystals is observed in the PC run products from "bottom-up" versus "top-down experiments. The "bottom-up" experiments produced numerous, euhedral small olivine crystals (<30 μm; Fig. 2c and 2e), whereas the "top-down" experiments formed large, sparse olivine crystals (>100 μm; Fig. 2d and 2f), with rapid-growth hopper textures (i.e., large melt hollows inside crystal).

None of the 1-bar experimental run products contained quench crystals. The only PC run products that contained quench crystals (≤3 mm snowflake shape; Fig. 2c and 2e) are those from the hydrous "bottom-up" experiments (PC-10 and PC-12; Table 3), which also had higher H_2O contents measured in the glass (4.0 and 4.3 wt%).

Compositions of olivine and glass

The average glass and olivine compositions, together with 1σ standard deviations in the oxide analyses, are reported for each run product in Table 4. All microprobe analyses on olivine and glass are reported in Appendix D and E, respectively, and the laser ablation analyses of Ni in glass is reported in Appendix F. In all cases, glass compositions were analyzed both immediately adjacent to and ≥ 50-100 μm further away from co-existing olivine crystals. No gradients in glass composition were detected as a function of distance from olivine crystals. In the two samples with quench crystals, there were always some relatively wide regions of glass between large olivine crystals and quench crystals (Fig. 2c and 2e), which enabled successful microprobe and laser ablation analyses.

For olivine, the MgO compositional variation is small (0.1-0.4 mol% Fo). For the glass, the variation in wt% MgO (± 0.19 wt% on average) is larger than the analyzed variation in the starting glass material (Table 2). This demonstrates real compositional variability within the glass, which is expected given the growth of olivine crystals. The combined variability in the

441 analyzed olivine and glass compositions leads to a propagated uncertainty in $D_{Mg}^{ol/liq}$ of 1-3% in
442 the 1-bar experiments and ±1-2% in the PC experiments (Table 3). Importantly, there is no
443 significant difference in the analytical error in $D_{Mg}^{ol/liq}$ between the 1-bar and PC experiments.
444 The average uncertainty in $D_{Mg}^{ol/liq}$ for all experiments is <2 % relative.
445 A similar assessment of homogeneity with respect to analyzed Ni contents in olivine and
446 glass in all run products was also made (Table 3). In the glass, the Ni concentrations in the
447 quenched glass in each run product vary by 3-11% relative, which is less than the two standard
448 deviation analytical error of the LA-ICP-MS method. A comparison of Ni contents analyzed in
449 the quenched glasses with the electron microprobe and with laser-ablation ICP-MS is shown in
450 Figure 3; the results show a strong 1:1 relationship (R^2 = 0.87), although the laser-ablation
451 analyses have significantly less error. The combined variability in the analyzed olivine and
452 glass composition contributes a relative uncertainty in $D_{Ni}^{ol/liq}$ of ±6-19% in the 1-bar experiments
453 and ±8-16% in the PC experiments (Table 3). Again, there is no significant difference in the
454 analytical error in $D_{Ni}^{ol/liq}$ between the 1-bar and PC experiments. The average uncertainty in
455 $D_{Ni}^{ol/liq}$ for all experiments in this study is ±11% relative.
456
457 *Phase proportions*
458 The phase abundances in the experimental run products (Table 3) were determined
459 using the non-linear least-square fitting approach of Albarède and Provost (1977), using the
460 composition of the glass and mineral phases in each experimental product (Table 4) as well as
461 the composition of the starting glass (Table 2). In all 1-bar experiments, olivine is the only
462 silicate mineral phase present and the amount of glass is ≥96%. In the four runs held at 1225
463 °C for 12-24 hours, the olivine abundance ranges from 0.3-1.7%, whereas in the two runs held
464 at 1200°C for 8-24 hours, the abundance of olivine is higher at 1.8-4.2% (Table 3a**).**
465 In seven of the nine PC experiments, olivine is the only silicate mineral phase and the
466 amount of glass is > 95%. Trace orthopyroxene is found in one hydrous top-down experiment

(PC-14). This is also the sample that lost the most H_2O during the experiment (Table 3b). In another experiment (PC-33; bottom-up, anhydrous, held for 48 hours at 1180 °C), 13% plagioclase crystallized together with 8% olivine. It is notable that the run product for PC-35, an experiment performed under identical conditions as that for PC-33 except for a shorter dwell time (29.5 hours), contains only 2% olivine and 98% glass. One possibility is that the PC-35 experiment did not reach the target pressure of 0.5 GPa, but instead attained a somewhat lower pressure (~0.4 GPa), thus lowering its liquidus temperature. Another possibility is that there was a kinetic hindrance to nucleation and crystallization that affected the amount of olivine and plagioclase that grew in that experiment. This highlights one of the key questions posed in this study: can there be a close approach to chemical equilibrium between olivine and melt when there is not an equilibrium abundance of olivine (or other mineral phases), owing to kinetic delays in nucleation and crystal growth?

Fe and Ni gain/loss

With the phase proportions in hand, mass-balance calculations allow an evaluation of the relative change in bulk Fe and Ni content after each experiment, due to Fe and Ni loss to or gain from the Au-Pd wire or capsule. For the 1-bar experiments, the change ranges from 0 to +1% (average <1%) for Fe, and -20% to +6% (average -6%) Ni (Table 3a). Those samples that lost more Ni to the wire were those held for longer time periods (e.g. 24 vs. 12 hours) and/or higher temperatures (1225 vs. 1200 °C). For the PC experiments, the change ranges from -1 to +11% relative for Fe (average +5%), whereas -26% to +33% Ni to the Au-Pd capsules (average -1%; Table 3b**).** There is no correlation between the extent of Fe and/or Ni loss (or gain) and the extent of analyzed variability in $D_{Mg}^{ol/liq}$ and/or $D_{Ni}^{ol/liq}$ (Table 3**).**

Analyzed H_2O concentrations in quenched glasses

The H_2O concentrations (± 5% relative) in the quenched glasses from the high-pressure experiments, which were analyzed by FTIR spectroscopy, are tabulated in Table 3. When analyzed wt% H_2O contents are combined with the electron microprobe analyses, the totals for the analyzed glasses range from 98.6-100.4 wt%, with an average of 99.5 wt% (Table 4). The FTIR results confirm that the glass in the two nominally anhydrous PC experimental run products contained 0.2 wt% H_2O. In contrast, the PC run products designed to contain ~5 wt% H_2O lost variable amounts of water, with quenched concentrations that range from 4.3 to 2.0 wt%. The "bottom-up" hydrous experiments lost less H_2O, whereas the "top-down" hydrous experiments that were held for the longest durations above their liquidus lost more H_2O.

The most common mechanism for H_2O loss in fluid-undersaturated melts held in Au-Pd capsules is through H_2 diffusion from the sample through the capsule wall, which is expected to drive oxidation in the melt (e.g. Hall et al., 2004). Another possible mechanism is diffusion of molecular H_2O through the capsule wall (Patiño Douce and Beard, 1994). In order to evaluate which of these mechanisms may have led to H_2O loss in the experimental melts in this study, an evaluation of melt oxidation state in the experimental samples and whether it correlates with H_2O loss is required.

Melt Fe^{3+}/Fe^{T} ratios and calculation of $^{Fe2+-Mg}K_D$ (olivine-liq)

Melt Fe^{3+}/Fe^{T} ratios can be calculated for all 1-bar experiments, since they were conducted under controlled fO_2 conditions (Table 3). In this study, the Kress and Carmichael (1991) model was used to be consistent with MELTS (Ghiorso and Sack, 1995; Asimow and Ghiorso, 1998). With the Fe^{2+} concentration in the melt phase calculated, values of $^{Fe2+-Mg}K_D$ (olivine-liq) were obtained for each of the six 1-bar experiments (Table 3a). For the three experiments that followed the "bottom-up" trajectory, the average (± 1σ) $^{Fe2+-Mg}K_D$ is 0.35 ± 0.01. For the single experiment (#23-2) that was conducted at ΔNNO = +2, the $^{Fe2+-Mg}K_D$ is 0.34 and is within analytical uncertainty of the other two values. For the remaining three experiments that

518 followed the "top-down" trajectory, the average (± 1σ) $^{Fe2+-Mg}K_D$ value is 0.36 ± 0.01, which is
519 within error of the "bottom-up" values. All these experimental values match the $^{Fe2+-Mg}K_D$ value
520 of 0.35 calculated with MELTS (Ghiorso and Sack, 1995; Asimow and Ghiorso, 1998) for the
521 olivine liquidus at ΔNNO = 0, using the UR-46 starting glass material (Table 2).
522 For the PC experiments, fO_2 was not buffered. Therefore, an evaluation of the Fe^{3+}/Fe^T
523 ratios in the quenched glasses of the experimental run products requires a direct measurement,
524 which was obtained on three of the PC run products using micro-XANES spectroscopy. Two of
525 the analyzed run products are from bottom-up experiments (anhydrous PC-33 and hydrous PC-
526 10), whereas the third is from a top-down experiment (hydrous PC-14).
527 For the two bottom-up experiments, the resulting Fe^{3+}/Fe^T ratios are strikingly different.
528 For the anhydrous run held for 48 hours at 1180°C, the Fe^{3+}/Fe^T ratio is 0.26, whereas for the
529 hydrous run held for 12 hours at 1125 °C, the Fe^{3+}/Fe^T ratio is 0.48. Despite these differences
530 in quenched oxidation state, when each respective ferric-ferrous ratio is combined with the
531 analyzed olivine composition in its run product, the two resulting $^{Fe2+-Mg}K_D$ values are within
532 analytical error of one another (0.35 ± 0.01 and 0.32 ± 0.02). For the top-down hydrous
533 experiment PC14, the analyzed Fe^{3+}/Fe^T ratio is 0.31, which leads to a $^{Fe2+-Mg}K_D$ value of 0.33 ±
534 0.01. All three $^{Fe2+-Mg}K_D$ values broadly match expected equilibrium values.
535
536 *Variation in melt Fe^{3+}/Fe^T ratios in experimental run products with run duration and H_2O loss*
537 A possible explanation for the different quenched oxidation states in the two bottom-up
538 run products can be seen in Figure 4, which illustrates a consistent trend of decreasing Fe^{3+}/Fe^T
539 ratio in the melt phase with increased duration (and temperature) of the experimental run. Note
540 that the starting glass in all experiments was highly oxidized (equilibrated at 1450 °C in air). For
541 a quench temperature of ≤1450 °C, the calculated melt Fe^{3+}/Fe^T is ≥ 0.64 (Kress and
542 Carmichael, 1991). For the two bottom-up run products that were not analyzed by micro-
543 XANES (PC-35 and PC-12), the melt Fe^{3+}/Fe^T can be estimated from the analyzed olivine

composition for an assumed $^{Fe2+-Mg}K_D$ value. If the average of the two values from PC-33 and PC-10 is used ($^{Fe2+-Mg}K_D$ =0.34), the calculated Fe^{3+}/Fe^T ratios are 0.34 and 0.47, respectively, and fall along the trend line in Figure 4**.** It thus appears that the initially oxidized starting glass became increasingly reduced with experimental run duration.

The cause of progressive reduction of the melt with run duration is most likely due to reaction of the melt by the Au-Pd-Fe capsule, which was pre-saturated under fO_2 conditions of ΔNNO = -1. This explanation is supported by the fO_2 recorded by the analyzed concentrations of Fe in the Au-Pd capsules (Appendix G), using the model calibrated by Barr and Grove (2010) that is based on the fO_2-dependence of Fe partitioning between AuPd metal and silicate melt. With increasing experimental time, the difference between the quenched redox state of the glass and that of the AuPd capsule decreased and converged after 48 hours (Fig.4).

An alternative mechanism to explain the trend in Figure 4, namely a higher quenched oxidation state in PC-10 (hydrous) compared to PC-33 (anhydrous), is by diffusion of H_2 through the capsule wall, leading to a loss of H_2O (PC-10 lost ~1 wt%) and thus an increase in oxidation state (e.g. Hall et al., 2004). However, this mechanism does not explain the analyzed Fe^{3+}/Fe^T ratio of 0.309 measured by micro-XANES in PC-14 (hydrous, top-down experiment), which lost ~ 2 wt% during its experimental run (Table 3). When the PC-14 ferric-ferrous ratio is combined with its analyzed olivine composition (Table 4), the resulting $^{Fe2+-Mg}K_D$ value is 0.33, which matches what is expected for olivine-melt equilibrium. It also overlaps the two $^{Fe2+-Mg}K_D$ values for the bottom-up experiments. In this top-down experiment, a greater loss of H_2O is not associated with a higher oxidation state, and therefore diffusion of H_2 from the sample through the capsule wall does not appear to explain the loss of H_2O in PC-10.

Another possibility for how H_2O may be lost in fluid-undersaturated PC experiments was suggested by Patiño Douce and Beard (1994), which is that molecular H_2O could plausibly diffuse from the sample across the metal capsule, albeit at slower rates than H_2. The data from this study suggest that the loss of H_2O in the top-down experiments largely occurred during the

570 dwell at super-liquidus temperatures (i.e., the hydrous bottom-up experiments lost the least
571 H_2O; Table 3).

572 For the purposes of this study, and for applications to natural basalts, the most important
573 observation is that the direct analyses of the Fe^{3+}/Fe^{T} ratio in the glass phase of three PC run
574 products all lead to $^{Fe2+-Mg}K_D$ (olivine-liq) values (=0.32-0.35) that are consistent with a close
575 approach to olivine-melt Fe-Mg exchange equilibrium. This is a key result because the three
576 PC experiments in question (PC-33, PC-10 and PC-14) underwent significantly different
577 histories with respect to change in oxidation state (relative to starting glass) and H_2O loss.
578

579 **Natural samples: whole-rock and olivine compositions**

580 The major-element compositions of the two K-rich basanite samples from the small-
581 volume cinder cones of Apaxtapec and La Erita in the Mexican arc (part of the Colima cones
582 suite; Carmichael et al., 2006; Pu, 2018) are reported in Table 5**,** together with whole-rock Ni
583 concentrations. Histograms of olivine analyses of phenocrysts from each sample are shown in
584 Figure 5a-b, and the most Fo-rich composition is reported in Table 5. Also shown (Fig. 5c-d)
585 are plots of analyzed Ni concentrations in olivine phenocrysts as a function of analyzed Fo
586 (forsterite) content. A linear fit to the olivine analyses that span highest 3 mol% Fo content
587 allow the average NiO content of the most Fo-rich olivine to be calculated. As explained in Pu
588 et al. (2017), the purpose of the linear fit is to obtain the most accurate estimate of the NiO
589 content of the most Fo-rich olivine (reported in Table 5), given that analytical uncertainties in
590 NiO lead to 1σ standard deviations of ≤ 0.05 wt%.

591 BSE images of olivine phenocrysts from these two samples are shown in Figure 6,
592 including those that are the most Fo-rich. The crystals display diffusion-limited growth textures,
593 including hopper and dendritic features, consistent with rapid growth during magma ascent (Pu
594 et al., 2017).
595

This is the peer-reviewed, final accepted version for American Mineralogist, published by the Mineralogical Society of America.
The published version is subject to change. Cite as Authors (Year) Title. American Mineralogist, in press.
DOI: https://doi.org/10.2138/am-2020-7014. http://www.minsocam.org/

DISCUSSION

Application of olivine-melt thermometers to experimental run products

One of the primary objectives of this study is to evaluate to what extent olivine-melt thermometers based on the partitioning of Mg^{2+} and Ni^{2+} can recover the experimental temperatures from this study, including those performed under hydrous conditions. To perform this evaluation, the analyzed values of $D_{Mg}^{ol/liq}$ and $D_{Ni}^{ol/liq}$ obtained for each of the six 1-bar experiments and nine PC experiments (two anhydrous and seven hydrous), were combined with the respective analyzed glass compositions (Table 3 and 4**)** to calculate temperature using the Mg- and Ni-based thermometers of Pu et al. (2017; see Eq.1, Table 1), which have model 1σ errors of ±26 and ±29 °C, respectively. The H_2O-corrected Mg-thermometer of Putirka et al (2007) was also applied to all experimental run products in this study. The results from all three thermometers are given in Table 6. Also reported are propagated errors in calculated temperatures from the ± 1σ analytical uncertainty in $D_{Mg}^{ol/liq}$ and $D_{Ni}^{ol/liq}$ (Tables 2 and 6). The analytical errors in calculated temperature range from ±4-9 °C for T_{Mg} and from ±13-46 °C for T_{Ni}**;** the respective average uncertainties are ±5 and ±25 °C.

Application of anhydrous Mg-thermometer (Pu'17) to experimental results

For the 1-bar experiments, the average deviation between calculated T_{Mg} (from anhydrous model of Pu et al., 2017) and experimental temperature ranges from +7 and +32°C, with an average difference of +14 °C. There is no systematic difference in the magnitude or sign of the residuals between the "bottom-up" and "top-down" experiments (Table 6). For the two anhydrous PC experiments (held for 48 and 29.5 hours,) the residuals are +6 and +26 °C, which suggests that the pressure correction of Herzburg and O'Hara (2002) is not resolved at 0.5 GPa; otherwise, the residuals would increase by an additional 26 °C.

For the hydrous PC experiments, the Mg-thermometer of Pu et al. (2017) significantly overestimates experimental temperature, with deviations that range from +49˚C to +127˚C (Table 6), well outside analytical and thermometer errors. The results are illustrated in Figure 7a and are fully consistent with experimental evidence from the literature that dissolved water in the melt strongly affects $D_{Mg}^{ol/liq}$ (e.g. Almeev et al., 2007; Medard and Grove, 2008).

Application of anhydrous Ni-thermometer (Pu'17) to experimental results

The key question that motivated this study is whether the Ni-thermometer of Pu et al. (2017) can successfully recover the temperatures of olivine-melt equilibrium experiments conducted under both anhydrous and hydrous conditions, without any correction for H_2O content. For the 1-bar experiments in this study, the average deviation between calculated T_{Ni} and experimental temperature ranges from -26 and +13°C, with an average difference of -13 °C (Table 6). For the two anhydrous PC experiments, the deviation is -1 and -32 °C, which again suggests that a pressure correction is not resolved at 0.5 GPa for the Ni-based olivine-melt thermometer. For the seven hydrous experiments, the Ni-thermometer of Pu et al. (2017) recovers the experimental temperatures notably well, with deviations that range from -18 to +39 °C, and an average difference of +3 °C (Table 6). A comparison of the calculated T_{Ni} values versus the experimental temperatures is illustrated in Figure 7b. Importantly, there is no clear difference in the sign or magnitude of the residuals between bottom-up and top-down experiments; this result is expected if loss of H_2O during olivine crystallization has no effect on $D_{Ni}^{ol/liq}$ values.

Application of H_2O-corrected Mg-thermometer (Putirka'07) to experimental results

In order to address the effect of H_2O in the melt on $D_{Mg}^{ol/liq}$, Putirka et al. (2007) calibrated a Mg-based olivine-melt thermometer that includes a correction for H_2O in the melt. As seen in Figure 7c, when this thermometer (Eq. 4 from Putirka et al., 2007) is applied to a set

of analyzed run products from 32 hydrous (≤5.7 wt% H_2O), near-liquidus (<5% olivine), olivine-melt equilibrium experiments from eight published studies (Sisson and Grove, 1993a, 1993b; Wagner et al., 1995; Moore and Carmichael, 1998; Berndt et al., 2005; Almeev et al., 2007; Medard and Grove, 2008; Parman et al., 2011) featured in Pu et al. (2017; Fig. 9 of that study), there is a close recovery of experimental temperatures, with an average (±1σ) deviation of -3 (±12) °C. For the compiled information on these 35 experiments from the literature, including H_2O water content in the melt phase, see Appendix L from Pu et al. (2017). Among the 35 experiments from the literature, three are from Moore and Carmichael (1998), for which the run products were analyzed for the Ni contents in olivine and glass by Pu et al. (2017).

Also shown in Figure 7c is a comparison of the experimental temperatures from this study to those calculated with the H_2O-corrected Mg-thermometer of Putirka (2007; Eq. 4), using the analyzed H_2O contents (≤ 4.3 wt%) in the run products (Table 6). For the 1-bar experiments, the average deviation between H_2O-corrected T_{Mg} and experimental temperature ranges from -3 and +21°C, with an average difference of +3 °C. For the two anhydrous PC experiments, the deviation is -2 and +13 °C; again, there is no evidence that a pressure correction (e.g. Herzberg and O'Hara, 2002) is experimentally resolved at 0.5 GPa. For the hydrous experiments, the H_2O-corrected Mg-thermometer of Putirka et al. (2007) recovers the experimental temperatures within analytical error, with an average difference of +10 °C (Table 6). It is noteworthy that the results in Figure 7c show a systematic difference in the sign of the residuals between the top-down and bottom-up experiments, which raises the question of whether some of the H_2O loss in the top-down experiments occurred during olivine crystallization and affected the equilibrium value of $D_{Mg}^{ol/liq}$. This may have led to olivine compositions in the top-down run products that reflect an approach to equilibrium that was not fully attained due to on-going H_2O loss. Despite this possibility, the temperature residuals for the top-down experiments are not large and most are within analytical error. Collectively, the results in Figure 7c illustrate the broad success of the H_2O-corrected Mg-thermometer of Putirka

et al. (2007; their Eq. 4) as long as a correction for H_2O the melt phase can be made. Unfortunately, this is not always the case for natural samples, because the H_2O analyses in olivine-hosted melt inclusions are not always available.

Direct comparison between Ni-thermometer and H_2O-corrected Mg-thermometer

It is also of interest to directly compare the calculated temperatures from the Ni-thermometer of Pu et al. (2017) to the calculated temperatures from the H_2O-corrected Mg-thermometer of Putirka et al. (2007) on a common set of experiments. The only available hydrous experimental data for this comparison are the seven experiments from this study, as well as the three olivine-melt equilibrium experiments from Moore and Carmichael (1998), for which Ni analyses of the glass and olivine in the run products were presented in Pu et al. (2017). The comparison (Fig. 8) shows that the average deviation between the two sets of thermometry results is -10 °C when applied to all 15 experiments from this study, and -7 °C when applied to the seven hydrous experiments. For the three hydrous experiments from Moore and Carmichael (1998), the differences between the two thermometers are -10, -39 and +66 °C, respectively, with an average difference of -6 °C. In summary, the results illustrated in Figures 7 and 8 support the hypothesis presented in Pu et al. (2017) that an olivine-melt thermometer based on $D_{Ni}^{ol/liq}$ can be applied to hydrous basalts to obtain temperature without requiring a priori knowledge of the H_2O content in the melt phase. The implication is that $D_{Ni}^{ol/liq}$ is insensitive to dissolved H_2O in the melt phase, unlike the case for $D_{Mg}^{ol/liq}$.

Evidence for different coordination numbers for Ni^{2+} and Mg^{2+} in silicate melts

Cause for negligible dependence of $D_{Ni}^{ol/liq}$ on dissolved water in the melt at crustal conditions

Pu et al. (2017) proposed that the reason Ni^{2+} is less sensitive than Mg^{2+} to dissolved water in the melt is due to a systematic difference in their respective average oxygen coordination numbers. It is well established in the spectroscopic literature that the average

698 oxygen coordination of Mg^{2+}, an alkaline earth metal, in quenched model basalt liquids is > 5,
699 with a significant population of 6-fold coordinated Mg^{2+} (e.g. George and Stebbins, 1998). In
700 contrast, transition metals like Ni^{2+} and Fe^{2+}, despite having the same valence and similar ionic
701 radii (0.69 and 0.78 nm, respectively) as Mg^{2+} (0.72 nm), have a systematically lower
702 coordination number (between 4- and 5-fold) in quenched model basalt liquids (e.g. Galoisy and
703 Calas, 1993). The most relevant spectroscopic study that constrains the coordination of Ni^{2+} in
704 hydrous magmatic melts is based on XAFS (X-ray absorption fine structure) experiments
705 performed at a synchrotron beamline under *in-situ* high-temperature (780 °C) and high-pressure
706 (520 MPa) conditions in a hydrothermal diamond anvil cell (Muñoz et al., 2005). In that study,
707 the resulting Ni K-edge XANES (X-ray absorption near-edge structure) spectra show that Ni^{2+} is
708 in 4-fold coordination (i.e., occurs as NiO_4 moieties) in hydrous rhyolite melt. Moreover, 4-fold
709 coordinated Ni^{2+} is found in similar melts that are anhydrous (Muñoz, 2003), which led Muñoz et
710 al. (2005) to conclude that dissolved water does not alter the local structural environment of Ni^{2+}
711 in rhyolitic melts. Although in-situ spectroscopic data on the Ni^{2+} coordination in hydrous
712 basaltic melts are not yet available, comparisons of its coordination environment in melts vs.
713 glasses shows that lower-coordinated Ni^{2+} (and Fe^{2+}) is favored in melts relative to glasses
714 (Jackson et al., 2005).
715
716 *Cause for different pressure dependence for $D_{Ni}^{ol/liq}$ and $D_{Mg}^{ol/liq}$.*
717 Different coordination numbers for Ni^{2+} and Mg^{2+} in magmatic liquids at crustal depths
718 may also explain why increasing pressure affects $D_{Ni}^{ol/liq}$ and $D_{Mg}^{ol/liq}$ differently, which was
719 illustrated in Pu et al. (2017) on the basis of the high-quality experiments of Matzen et al.
720 (2013). Additional high-quality $D_{Ni}^{ol/liq}$ and $D_{Mg}^{ol/liq}$ equilibrium experiments at 1 bar and elevated
721 pressure were published by Matzen et al. (2017), which were unavailable at the time the Pu et
722 al. (2017) study was submitted for final publication. Here, the Ni- and Mg-thermometers of Pu
723 et al. (2017) are applied to all of the experiments from Matzen et al. (2013, 2017), which range

724 from 1-bar to 3 GPa. In a plot of temperature residual vs. pressure, a clear pressure effect is
725 seen for the Mg-thermometer (Fig. 9a). The solid line indicates the pressure correction from
726 Herzberg and O'Hara (2002), which was developed for use with the Beattie (1993) Mg-
727 thermometer. The results in Figure 9a illustrate that this pressure correction model works
728 equally well with the Pu et al. (2017) Mg-thermometer when applied to the high-pressure
729 Matzen et al. (2013, 2017) experimental results.

730 For the Ni-thermometer, the residuals illustrate a different behavior with changing
731 pressure (Fig. 9a). Although there is no evidence of a pressure dependence at < 1 GPa (i.e.,
732 crustal conditions), the onset of a pressure dependence develops at 1 GPa. In this study, a
733 polynomial fit to these data produces the following pressure correction to temperatures
734 calculated with the Pu et al. (2017) Ni-thermometer (T_{Ni}) that should only be applied between 1
735 and 3 GPa:

736 $$T_{Ni}(P) = T_{Ni} - 70 + 110*P(GPa) - 18*P(GPa)^2 \quad (2)$$

737 Extrapolation to higher pressures is strongly discouraged, and no pressure correction is
738 required at < 1 GPa. Application of Equation 2 recovers the temperatures from the high-
739 pressure experiments of Matzen et al. (2013, 2017) within +10 to -13 °C (- 1 °C, on average).
740 Application of the Matzen et al. (2017) model, which includes no pressure correction (on the
741 assumption that $D_{Ni}^{ol/liq}$ and $D_{Mg}^{ol/liq\ to}$ vary similarly with pressure, and thus the pressure term
742 cancels out), recovers their own experimental temperatures (Matzen et al., 2013; 2017) within
743 +52 to -103 °C (-20 °C on average; Fig. 9b).

744 As previously proposed in Pu et al. (2017), the delayed onset of a pressure dependence
745 to $D_{Ni}^{ol/liq}$ at 1 GPa (Fig. 9a) likely reflects the predominance of 4-fold coordinated Ni^{2+} at crustal
746 pressures, which changes to 6-fold coordination at mantle pressures (e.g. Jones et al., 2011).
747 If the onset of a pressure dependence marks the emergence of a significant proportion of 6-fold
748 Ni^{2+} (due to pressure-induced coordination change), it may also mark the onset of a
749 dependence of $D_{Ni}^{ol/liq}$ on dissolved water in the melt. The prediction of Pu et al. (2017) that

750 $D_{Ni}^{ol/liq}$ may develop a sensitivity to dissolved water in the melt at > 1 GPa, owing to the
751 presence of six-fold coordinated Ni^{2+}, is a testable hypothesis that can be evaluated in future
752 experimental studies.
753
754 *Cause for different anhydrous melt compositional dependence for $D_{Ni}^{ol/liq}$ and $D_{Mg}^{ol/liq}$.*
755 Spectroscopic evidence that Ni^{2+} and Mg^{2+} have different coordination numbers not only
756 explains why $D_{Ni}^{ol/liq}$ and $D_{Mg}^{ol/liq}$ have a different dependence on pressure and dissolved H_2O
757 concentration in the melt, but also explains the difference in their dependence on anhydrous
758 melt composition, which is clearly seen in a comparison of the fitted compositional parameters
759 for the Ni- and Mg-based olivine-melt thermometers, respectively (Table 1). Because both the
760 Ni- and Mg-based olivine-melt thermometers of Pu et al. (2017) were calibrated on the same 1-
761 bar experimental data set, a comparison of their respective fitted compositional terms (Table 1)
762 is revealing. Although the fitted values for *a* and *b* are within 1σ uncertainty of each other, those
763 for *c*, *d* and *e* are not. The largest difference is between the fitted values for *d* (modifies the
764 X_{SiO2} term), which differ in sign and magnitude (by a factor of two) between the two models. The
765 cause for this distinctly different dependence that $D_{Ni}^{ol/liq}$ and $D_{Mg}^{ol/liq}$ have on anhydrous melt
766 composition is readily explained by their different average coordination numbers at 1 bar.
767 A corollary to this finding is that models of $D_{Ni}^{ol/liq}$ that are based on the Ni-Mg exchange
768 reaction between olivine and melt under the assumption that composition affects $D_{Ni}^{ol/liq}$ and
769 $D_{Mg}^{ol/liq}$ similarly, and thus cancels out when fitting for the Ni-Mg exchange partition coefficient $K_{D,Ni\text{-}Mg}^{ol/liq}$, may require re-evaluation. This was the approach taken in Matzen et al. (2017),
771 where the form of their model equation, $\ln[(D_{Ni}^{ol/liq})/(D_{Mg}^{ol/liq})] = a + b/T(K)$, excludes compositional
772 terms, as well as a pressure correction. A test of whether compositional terms can be omitted,
773 on the assumption that they are broadly the same for $D_{Ni}^{ol/liq}$ and $D_{Mg}^{ol/liq}$ and thus cancel, is
774 made by evaluating how well the Matzen et al. (2017) thermometer recovers the 123 1-bar
775 experiments used to calibrate the Pu et al. (2017) thermometers (Fig. 10c). Also shown are

residuals for the six 1-bar experiments from this study, which range from -13 to +46 °C, and the four 1-bar experiments from Matzen et al. (2017), which range from +4 to +72 °C (Fig. 10c). For comparison, the Pu et al. (2017) Ni-thermometer recovers these two sets of data within -27 to +14 °C and -15 to +23 °C, respectively (Fig. 10a). Additionally, the Pu et al., (2017) Mg-thermometer recovers these two sets of data equally well as the Ni-thermometer (Fig. 10b).

The Matzen et al. (2017) model was calibrated on a different, though overlapping, experimental data set from that employed by Pu et al. (2017). One important difference is that the Matzen et al. (2017) model was calibrated on high-pressure experiments, both their own and those from the literature that passed their quality-assessment filters. Therefore, an evaluation of whether the difference in residuals between Figures 10a and 10c is caused by a difference in calibration datasets is made by re-fitting the form of the Matzen et al. (2017) equation on the same set of 1-bar experiments used by Pu et al. (2017). The results (Appendix H) show that the difference in residuals between the two studies (Fig. 10) is due to the form of the model equation (i.e., inclusion vs. exclusion of fitted compositional terms) and not the calibration data set.

In summary, because Ni^{2+} and Mg^{2+} have different coordination numbers in crustal magmatic melts, it is necessary for Ni- and Mg-based olivine-melt thermometers to account for these differences. The evidence from this study shows that the Ni-thermometer of Pu et al. (2017) is independent of dissolved water in the melt and crustal pressure, which allows it to be applied to hydrous, subduction-zone basalts that have crystallized olivine phenocrysts at crustal depths.

Application of Ni-based olivine-melt thermometer to hydrous basalts

In order to test the application of the Ni-thermometer to hydrous arc basalts, Pu et al. (2017) examined three calc-alkaline arc lavas (JOR-44, TAN-19, APA-6) erupted from the Michoacán-Guanajuato segment of the Mexican arc, which were previously described by Luhr

and Carmichael (1981) and Ownby et al. (2011). Importantly, these three lavas were erupted from scoria cones that were sampled by Johnson et al. (2008, 2009) in a study of olivine-hosted melt inclusions and their volatile contents. The rapid-growth textures (i.e., dendritic and hopper) in the olivine phenocrysts from those three lavas led Pu et al. (2017) to postulate that they crystallized during ascent, driven by H_2O-degassing (similar to the documented case for plagioclase phenocrysts in crystal-poor low-SiO_2 rhyolites; Waters et al., 2015). Pu et al. (2017) further proposed that the most Fo-rich olivine analyzed in each sample may closely approximate the equilibrium composition to first crystallize from the bulk liquid. In other words, if most (or all) of the phenocryst growth in each sample occurred during ascent, the whole-rock composition of the erupted lava may closely match that of the bulk liquid from which the first olivine crystallized.

On this basis, Pu et al. (2017) analyzed the olivine phenocryst population in each sample and picked the most Fo-rich for olivine-melt thermometry. The bulk composition of the whole-rock was used for the melt composition. The data employed by Pu et al. (2017) for the application of olivine-melt thermometry, based on $D_{Ni}^{ol/liq}$ and $D_{Mg}^{ol/liq}$, to these three samples is summarized in Table 5. The olivine-melt thermometry results (Table 5) reveal a systematic difference in temperatures calculated with the anhydrous Mg- and Ni-based thermometers of Pu et al. (2017), which was attributed to the presence of H_2O in these samples, causing T_{Mg} to overestimate temperature. Pu et al. (2017) showed that when the H_2O-corrected Mg-thermometer of Putirka et al. (2007) was applied to these three samples, using the data summarized in Table 5, which includes the maximum H_2O contents analyzed in olivine-hosted melt inclusions from these three lavas (from Johnson et al., 2008, 2009), the resulting temperatures broadly match those calculated with the Ni-based thermometer (Table 5), within the combined error of the two thermometers. This observation supports the hypothesis that the Ni-thermometer does not require a correction for H_2O when applied to hydrous, calc-alkaline basalts.

In this study, a comparison between the Ni-thermometer of Pu et al. (2017) and the H_2O-corrected Mg-thermometer of Putirka et al. (2007) is made on two additional natural samples, namely the two K-rich basanites from the Colima cones (Table 5). For the application of olivine-melt thermometry, it is assumed that the most Fo-rich olivine in each sample closely represents the first olivine to crystallize from a liquid with a composition close to that of the whole-rock sample. This is a reasonable hypothesis for a mantle-derived melt that ascended directly to the surface via transport along a fracture, without stalling in a crustal chamber. The diffusion-limited growth textures in the olivine phenocrysts (Fig. 6**)** support this hypothesis.

When the anhydrous Mg- and Ni-based thermometers of Pu et al. (2017) are applied to these two K-rich basanites, there is a systematic difference in the calculated temperatures, with T_{Mg} values 75 and 128 °C higher than T_{Ni} values (Table 6). When the H_2O-corrected Mg-based thermometer of Putirka et al. (2007) is applied, utilizing the maximum H_2O contents (6.2 and 6.7 wt%; Table 5) analyzed in olivine-hosted melt inclusions (Vigouroux et al., 2008; Maria and Luhr, 2008), the resulting temperatures closely match those of the Ni-based thermometer (Fig. 8). The differences in calculated temperatures for COL-1001 (Apaxtepec) and COL-1015 (La Erita), are -28 and -25 °C, respectively, and thus show close agreement (Fig. 8; Table 5). Collectively, the results from all five natural samples all strongly support the evidence that the Ni-thermometer of Pu et al. (2017) does not require a correction for H_2O content (or crustal pressures; Fig. 9a) in order to give accurate temperatures that match those of the H_2O-corrected Mg-thermometer of Putirka et al. (2007).

Implications

The experimental results from this study show that the Pu et al. (2017) olivine-melt thermometer based on $D_{Ni}^{ol/liq}$ (and the updated version from this study), calibrated on 1-bar, anhydrous melts, recovers experimental temperatures of all hydrous (≤4.3 wt% H_2O), high-

853 pressure (0.5 GPa) experiments conducted in this study. In contrast, application of olivine-melt
854 thermometers based on $D_{Mg}^{ol/liq}$ to the same hydrous experiments leads to temperatures that
855 are too high, consistent with a strong dependence of $D_{Mg}^{ol/liq}$ to melt water contents, as
856 previously discussed in the literature (e.g. Almeev et al., 2007; Putirka et al., 2007; Medard and
857 Grove, 2008). Therefore, the utility of applying an H_2O-independent olivine-melt thermometer
858 (i.e., based on $D_{Ni}^{ol/liq}$) to natural hydrous basalts is two-fold.

859 The first advantage of the Ni-thermometer is that it circumvents the need to obtain
860 independent determinations of melt water contents during olivine growth, in order to obtain
861 accurate magmatic temperatures from thermometers based on $D_{Mg}^{ol/liq}$. Currently, the best
862 method to obtain melt water contents is through analyses of H_2O in olivine-hosted melt
863 inclusions. Although these data are invaluable, they typically only provide minimum H_2O values
864 owing to chronic problems of volatile loss during ascent and eruption, especially in effusive
865 lavas rather than those erupted explosively as scoria (e.g. Lloyd et al., 2013). Thus, it is difficult
866 to obtain large, global data sets of temperature on the basis of Mg-based olivine-melt
867 thermometers, in order to evaluate how the temperature of hydrous arc basalts varies between
868 and among different subduction-zone segments around the world. Application of the Ni-based
869 olivine-melt thermometer, which does not require independent information on melt water
870 contents, has the potential to generate these large data sets.

871 A second advantage of the Ni-thermometer is that it can be used in conjunction with the
872 H_2O-dependent Mg-thermometer to obtain a *qualitative* assessment of melt water contents,
873 which in turn can be compared to independent measurements of volatile contents from olivine-
874 hosted melt inclusions. Note that uncertainties in melt water contents lead to relatively small
875 propagated errors in the H_2O-corrected Mg-thermometer of Putirka et al. (2007). For example,
876 an uncertainty of ±1 wt% H_2O leads to an uncertainty in calculated temperature of ± 20 °C.
877 Although this leads to relatively small errors in temperature calculated with the H_2O-corrected
878 Mg-thermometer, the application of the anhydrous Ni- and Mg-thermometry as a hygrometer

cannot provide quantitative H_2O contents because propagated errors are too large. For example, an uncertainty in ΔT (=T_{Mg} - T_{Ni}) of ±29 °C (from the thermometers of Pu et al., 2017) will lead to an uncertainty in calculated H_2O content (using H_2O-corrected Mg-thermometer of Putirka et al., 2007) of ± 1.5 wt%.

The most useful application of the Ni-based olivine-melt thermometer to obtain melt water contents is through combined usage with the plagioclase-liquid hygrometer, which requires independent constraints on temperature. For example, Pu et al. (2017) applied the plagioclase-liquid hygrometer, in concert with the Ni-based olivine-melt thermometer, to two natural samples that were co-saturated with plagioclase and olivine at the liquidus. The reported calculated water contents (2.9 and 2.5 wt%) have a relatively low uncertainty of ± 0.4 wt%, due to the propagated uncertainty in T_{Ni} of ± 29 °C. Thus, application of the H_2O-independent olivine-melt thermometer based on $D_{Ni}^{ol/liq}$ greatly expands the opportunity to apply plagioclase-liquid hygrometry to basaltic andesite melts.

Acknowledgements

We thank Jean-Claude Barrette at the University of Windsor for his assistance during the numerous Laser-Ablation-ICP-MS analytical sessions for this study. The μ-XANES analyses of the experimental glasses was made possible through the generous support from Katherine Kelley and Elizabeth Cottrell, who also helped improve part of this manuscript. We also thank Anthony Lanzirotti and Matthew Newville for onsite support during the XANES analytical sessions. Youxue Zhang and Adam Simon shared some of their laboratory resources unsparingly, which enabled the successful experimental efforts in this study, and provided constructive comments on an earlier version of this work. Laura Waters provided vital suggestions that resolved some of the technical challenges in this project. Jameson Jolles helped with the thermal gradient calibration of the piston cylinder apparatus. This study was supported by National Science Foundation grant (EAR-1551344). The operational support for

GeoSoilEnviroCARS, Advanced Photon Source (APS), Argonne National Laboratory (The University of Chicago, Sector 13) was supported by the National Science Foundation - Earth Sciences (EAR-1634415) and Department of Energy (DOE) - GeoSciences (DE-FG02-94ER14466). Use of the APS facilities was supported by the DOE Office of Science by Argonne National Laboratory under Contract No. DE-AC02- 06CH11357. Constructive and insightful reviews by Andrew Matzen and Keith Putirka, and additional editorial comments by Charles Lesher, led to significant improvements of the manuscript.

References

Albarede, F. and Provost, A. (1977) Petrological and geochemical mass-balance equations: an algorithm for least-square fitting and general error analysis. Computers and Geosciences, 3, 309-326.

Allan, J.F., Batiza, R., Perfit, M.R., Fornari, D.J., and Sack, R.O. (1989) Petrology of lavas from the Lamont Seamount Chain and adjacent East Pacific Rise, 10°N. Journal of Petrology, 30, 1245–1298.

Almeev, R.A., Holtz, F., Koepke, J., Parat, F., Botcharnikov, R.E. (2007) The effect of H_2O on olivine crystallization in MORB: experimental calibration at 200 MPa. American Mineralogist, 92, 670-674.

Asimow, P.D., and Ghiorso M.S. (1998) Algorithmic modifications extending MELTS to calculate subsolidus phase relations. American Mineralogist, 83, 1127-1131.

Barr, J.A., and Grove, T.L. (2010) AuPdFe ternary solution model and applications to understanding the fO_2 of hydrous, high-pressure experiments. Contributions to Mineralogy and Petrology, 160, 631-643.

Beattie, P. (1993) Olivine-melt and orthopyroxene-melt equilibria. Contributions to Mineralogy and Petrology, 115, 103-111.

Berndt, J., Koepke, J., Holtz, F. (2005) An experimental investigation of the influence of water and oxygen fugacity on differentiation of MORB at 200 MPa. Journal of Petrology, 46, 135-167.

Carmichael, I.S.E., Turner, F.J. and Verhoogen, J. (1974) Igneous Petrology, 739p. McGraw-Hill, New York.

Carmichael, I.S.E., Frey, H.M., Lange, R.A., & Hall, C.M. (2006). The Pleistocene cinder cones surrounding Volcán Colima, Mexico re-visited: eruption ages and volumes, oxidation states, and sulfur content. Bulletin of Volcanology, 68(5), 407–419.

Cottrell, E., Kelley, K.A., Lanzirotti, A., and Fischer, R.A. (2009) High-precision determination of iron oxidation state in silicate glass using XANES. Chemical Geology, 268, 167-179.

Cottrell, E., Lanzirotti, A., Mysen, B., Birner, S.K., Kelley, K.A., Botcharnikov, R., Davis, F.A., and Newville, M. (2018) A Mössbauer-based XANES calibration for hydrous basalt glasses reveals radiation-induced oxidation of Fe. American Mineralogist, 103, 489-501.

Dixon, J.E., Stolper, E.M., and Holloway, J.R. (1995) An Experimental Study of Water and Carbon Dioxide Solubilities in Mid-Ocean Ridge Basaltic Liquids. Part I: Calibration and Solubility Models. Journal of Petrology, 36, 1607–1631.

Faure, F., and Schiano, P. (2005) Experimental investigation of equilibration conditions during forsterite growth and melt inclusion formation. Earth and Planetary Science Letters, 236, 882–898.

Galoisy, L., and Calas G. (1993) Structural environment of nickel in silicate glass/melt system: Part 1. Spectroscopic determination of coordination states. Geochimica et Cosmochimica Acta, 57, 3613-3626.

George, A.M., and Stebbins, J.F. (1998) Structure and dynamics of magnesium in silicate melts: A high-temperature ^{25}Mg NMR study. American Mineralogist, 83, 1022-1029.

Guillong, M., Meier, D.L., Allan, M.M., Heinrich, C.A., and Yardley, B.W.D. (2008) Appendix A6: SILLS: A Matlab-based program for the reduction of Laser Ablation ICP-MS data of homogeneous materials and inclusions. Mineralogical Association of Canada Short Course 40, Vancouver, B.C., p. 328-333.

Ghiorso, M.S., and Sack, R.O. (1995) Chemical mass transfer in magmatic processes. IV. A revised and internally consistent thermodynamic model for the interpolation and extrapolation of liquid-solid equilibria in magmatic systems at elevated temperatures and pressures. Contributions to Mineralogy and Petrology, 119, 197-212.

Hall, L.J., Brodie, J., Wood, B.J., and Carroll, M.R. (2004) Iron and water losses from hydrous basalts contained in $Au_{80}Pd_{20}$ capsules at high pressure and temperature. Mineralogical Magazine, 68(1), 75-81.

Hammer, J.E. and Rutherford, M.J. (2002) An experimental study of the kinetics of decompression-induced crystallization in silicic melt. Journal of Geophysical Research, 107, B1, 2021.

Herzberg, C., and O'Hara, M.J. (2002) Plume-associated ultramafic magmas off Phanerozoic age. Journal of Petrology, 43, 1857-1883.

Hui, H., and Zhang, Y. (2007) Toward a general viscosity equation for natural anhydrous and hydrous silicate melts. Geochimica et Cosmochimica Acta, 71, 403–416.

Jackson, W.E., Farges, F., Yeager, M., Mabrouk, P.A., Rossano, S., Waychunas, G.A., Solomon, E.I., and Brown, G.E. (2005) Multi-spectroscopic study of Fe(II) in silicate glasses: implications for the coordination environment of Fe(II) in silicate melts. Geochimica et Cosmochimica Acta, 69, 4315-4332

Johnson, E.R., Wallace, P.J., Cashman, K.V., Delgado-Granados, H., and Kent, A.J.R. (2008) Magmatic volatile contents and degassing-induced crystallization at Volcán Jorullo, Mexico: Implications for melt evolution and the plumbing systems of monogenetic volcanoes. Earth and Planetary Science Letters, 269, 478-487.

Johnson, E.R., Wallace, P.J., Granados, H.D., Manea, V.C., Kent, A.J.R., Bindeman, I.N., and Donegan, C.S. (2009) Subduction-related volatile recycling and magma generation beneath Central Mexico: Insights from melt inclusions, oxygen isotopes and geodynamic models. Journal of Petrology, 50, 1729-1764.

Jones, J., O'Neill, H.S., and Berry, A. (2011) Differential changes in Ni^{2+}, Co^{2+} and Fe^{2+} coordination in silicate melt with pressure. Goldschmidt Conference Abstract, Mineralogical Magazine, 75, 1124.

Kress, V.C., and Carmichael, I.S.E. (1991). The compressibility of silicate liquids containing Fe2O3 and the effect of composition, temperature, oxygen fugacity and pressure on their redox states. Contributions to Mineralogy and Petrology 108, 82-92.

Lange, R.A. (1997) Temperature independent thermal expansivities of sodium aluminosilicate melts between 713 and 1835 K: Erratum to R. A. Lange (1996) Geochimica et Cosmochimica Acta 60, 4989–4996 (1997)

Lange, R.A. and Carmichael, I.S.E. (1990) Thermodynamic properties of silicate liquids with an emphasis on density, thermal expansion and compressibility. In J. Nicholls and J.K. Russell, Eds., Modern Methods of Igneous Petrology: Understanding Magmatic Processes, 24, p. 25-64. Reviews of Mineralogy, Mineralogical Society of America, Chantilly, Virginia.

Langmuir, C.H., Bezos, A., Escrig, S. and Parman, S.W. (2006), Chemical systematics and hydrous melting of the mantle in back-arc basins. In D.M. Christie, C.R. Fischer, S-M. Lee and S. Givens, Eds., Back-Arc Spreading Systems: Geological, Biological, Chemical and Physical Interactions, 166, p. 87-146. Geophysical Monograph Series, American Geophysical Union, Washington, D. C.

Luhr, J.F., and Carmichael, I.S.E. (1981) The Colima volcanic complex, Mexico: Part II. Late-quaternary cinder cones. Contributions to Mineralogy and Petrology, 76,127–147.

Lofgren, G. (1974) An experimental study of plagioclase crystal morphology: isothermal crystallization. American Journal of Science, 274, 243-273.

Lloyd, A.S., Plank, T., Ruprecht, P., Hauri, E., and Rose, W. (2013) Volatile loss from melt inclusions in pyroclasts of differing sizes. Contributions to Mineralogy and Petrology, 165, 129–153.

Maria, A.H., and Luhr, J.F. (2008) Lamprophyres, basanites, and basalts of the western Mexican Volcanic Belt: volatile contents and a vein–wallrock melting relationship. Journal of Petrology, 49, 2123–2156.

Matzen, A.K., Baker, M.B., Beckett, J.R., and Stolper, E.M. (2013) The temperature and pressure dependence of nickel partitioning between olivine and silicate melt. Journal of Petrology, 54, 2521-2545.

Matzen, A.K., Baker, M.B., Beckett, J.R., Wood, B.J., and Stolper, E.M. (2017) The effect of liquid composition on the partitioning of Ni between olivine and silicate melt. Contributions to Mineralogy and Petrology, 172:3.

Médard, E., and Grove, T.L. (2008) The effect of H_2O on the olivine liquidus of basaltic melts: experiments and thermodynamic models. Contributions to Mineralogy and Petrology, 155, 417-432.

Moore, G., and Carmichael, I.S.E. (1998) The hydrous phase equilibria (to 3 kbar) of an andesite and basaltic andesite from western Mexico: constraints on water content and conditions of phenocryst growth. Contributions to Mineralogy and Petrology, 130, 304-319.

Moore, G., Roggensack, K., and Klonowski, S. (2008) A low-pressure-high-temperature technique for the piston-cylinder. American Mineralogist, 93, 48-52.

Muñoz, M. “Comportement d’´el´ements formateurs et modificateurs de r´eseau dans des magmas hydrat´es” (PhD thesis, Universit´e de Marne-La-Vall´ee, France 2003), p. 247.

Muñoz, M., Bureau, H., Malavergne, V., Menez, B., Wilke, M., Schmidt, C., Simionovici, A., Somogyi, A., and Farges, F. (2005) In-situ speciation of Nickel in hydrous melts exposed to extreme conditions. Physica Scripta, 115, 921-922.

Ni, H., Keppler, H., Walte, N., Schiavi, F., Chen, Y., Masotta, M., and Li, Z. (2014) In situ observation of crystal growth in a basalt melt and the development of crystal size distribution in igneous rocks. Contributions to Mineralogy and Petrology, 167, 1003.

Ochs, F.A., III, and Lange, R.A. (1999) The density of hydrous magmatic liquids. Science, 283, 1314–1317.

Ownby, S.E., Lange, R.A., Hall, C.M., and Delgado-Granados, H. (2011) Origin of andesite in the deep crust and eruption rates in the Tancítaro-Nueva Italia region of the central Mexican arc. Geological Society of America Bulletin, 123, 274-294.

Parman, S.W., Grove, T.L., Kelley, K.A., Plank, T. (2011) Along-arc variations in the pre-eruptive H2O contents of Mariana Arc magma inferred from fractionation paths. Journal of Petrology, 52, 257-278.

Patiño Douce, A.E., and Beard, J.S. (1994) H2O loss from hydrous melts during fluid-absent piston cylinder experiments. American Mineralogist, 79, 585-588.

Pearce, N.J.G., Perkins, W.T., Westgate, J.A., Gorton, M.P., Jackson, S.E., Neal, C.R., and Chenery, S.P. (1997) A compilation of new and published major and trace element data for NIST SRM 610 and NIST SRM 612 glass reference materials. Geostandards Newsletter, 21, 115–144.

Pu, X. (2018) New constraints on temperature, oxygen fugacity and H_2O of subduction zone basalts based on olivine-melt equilibrium. Ph.D thesis, University of Michigan.

Pu, X., Lange, R.A., and Moore, G. (2017) A comparison of olivine-melt thermometers based on D_{Mg} and D_{Ni}: The effects of melt composition, temperature, and pressure with applications to MORBs and hydrous arc basalts. American Mineralogist, 102, 750–765.

Putirka, K.D., Perfit, M., Ryerson, F.J., and Jackson, M.G. (2007) Ambient and excess mantle temperatures, olivine thermometry, and active vs. passive upwelling. Chemical Geology, 241, 177-206.

Putirka, K.D. (2008) Thermometers and barometers for volcanic systems. In K.D. Putirka and F.J. Tepley III, Eds., Minerals, Inclusions and Volcanic Processes, 69, p. 61-120. Reviews in Mineralogy and Geochemistry, Mineralogical Society of America, Chantilly, Virginia.

Sisson, T.W., and Grove, T.L. (1993a) Experimental investigations of the role of H_2O in calc-alkaline differentiation and subduction zone magmatism. Contributions to Mineralogy and Petrology, 113,143-166.

Sisson, T.W., and Grove, T.L. (1993b) Temperatures and H_2O contents of low-MgO high-alumina basalts. Contributions to Mineralogy and Petrology, 113, 167-184.

Tenner, T.J., Lange, R.A., and Downs, R.T. (2007) The albite fusion curve re-examined: New experiments and the high-pressure density and compressibility of high albite and NaAlSi3O8 liquid. American Mineralogist, 92, 1573-1585.

Vigouroux, N., Wallace, P.J., and Kent, A.J.R. (2008) Volatiles in High-K Magmas from the Western Trans-Mexican Volcanic Belt: Evidence for Fluid Fluxing and Extreme

Enrichment of the Mantle Wedge by Subduction Processes. Journal of Petrology, 49, 1589–1618.

Wagner, T.P., Donnelly-Nolan, J.M., Grove, T.L. (1995) Evidence of hydrous differentiation and crystal accumulation in the low-MgO, high Al_2O_3 Lake Basalt from Medicine Lake volcano, California. Contributions to Mineralogy and Petrology, 121, 201-216.

Waters, L.E., Andrews, B.J., Lange, R.A. (2015) Rapid crystallization of plagioclase phenocrysts in silicic melts during fluid-saturated ascent: phase equilibrium and decompression experiments. Journal of Petrology, 56, 981-1006.

Waters, L.E., and Lange, R.A. (2017) An experimental study of between orthopyroxene and rhyolite: a strong dependence on H2O in the melt. Contributions to Mineralogy and Petrology, 172, 1–13.

Zhang, Y., Belcher, R., Ihinger, P.D., Wang, L., Xu, Z., and Newman, S. (1997) New calibration of infrared measurement of dissolved water in rhyolite glass. Geochimica et Cosmochimica Acta, 61, 3089–3100.

Zhang, H.L., Cottrell, E., Solheid, P.A., Kelley, K.A., and Hirschmann, M.M. (2018) Determination of Fe3+/ ΣFe of XANES basaltic glass standards by Mössbauer spectroscopy and its application to the oxidation state of iron in MORB. Chemical Geology, 479, 166-175.

Figure captions

FIGURE 1. A schematic diagram shows how effective undercooling ($\Delta T_{eff} = T_{liquidus} - T_{melt}$) controls rates of crystal growth (dashed line) and nucleation (solid line) in supercooled liquids (modified from Carmichael et al, 1974). In the bottom-up trajectory of the experiments, the starting glass is heated above its glass transition temperature and transits, as a supercooled liquid, through a region of large undercooling, which corresponds to high nucleation and low crystal growth rates, resulting in numerous small crystals. In the top-down trajectory of the experiments, during rapid cooling from above the liquidus, the supercooled liquid transits a region of moderate undercooling, which is associated with low nucleation and high crystal growth rates, leading to sparse, large crystals.

FIGURE 2. Back-scattered electron (BSE) images of olivine textures in experimental run products. 1-bar experiments: **(a)** #22 and **(b):** #21-1; PC experiments: **(c)** PC10, **(d)** PC-13, **(e)** PC-12 and **(f)** PC14). On the left column (a,c,e) are bottom-up run products with relatively small crystals (≤10μm); on the right column (b,d,f) are top-down run products with larger crystals (>100μm).

FIGURE 3. Average Ni content in glass measured by laser-ablation (LA) ICP-MS vs. electron microprobe analyzer (EMPA) for all hydrous experiments reported in this study. The error bars are the standard deviations of all analyses on each run product (on average, ~7.6% for LA-ICP-MS and ~22.8% for EMPA).

FIGURE 4. Plot of Fe^{3+}/Fe^{T} ratio vs. experimental dwell time for all four bottom-up PC experiments: PC10, PC12 (hydrous); PC33, PC35 (no added H_2O). Red circles show Fe^{3+}/Fe^{T+} ratios analyzed by micro-XANES technique in glass of run products of PC10 and PC33. The black diamonds are calculated Fe^{3+}/Fe^{T+} ratios in glass for all four bottom-up PC experiments,

based on $^{Fe2+-Mg}K_D$ of 0.33 and average glass and olivine compositions (Table 4). These results match analyzed micro-XANES measurements. The blue symbols (at t=0) are the calculated Fe^{3+}/Fe^{T} of the starting glass equilibrated in air (blue circle) and equilibrated at ΔNNO =-1 (blue triangle); the latter is the pre-saturation run condition for all AuPd capsules. The green triangles are calculated glass Fe^{3+}/Fe^{T} ratios, based on fO_2 calculated from analyzed Fe content in Au-Pd capsules of run products (Barr and Grove, 2010). Open symbols are used for PC-12 to distinguish from PC-10. The collective data in this figure show that the high oxidation state of the initial starting glass (equilibrated in air) reacted with the Au-Pd capsule (pre-saturated at ΔNNO=-1) during the PC experiments, leading to a gradual decrease in glass Fe^{3+}/Fe^{T} ratios in the experimental charges with increasing run duration. Although the glass Fe^{3+}/Fe^{T} ratio requires 48 hours to fully equilibrated with the capsule (shown by PC33), it takes less than 12 hours to reach chemical equilibrium between glass and olivine (see the overlap of the black diamond and red circle in PC10). All calculations use Kress and Carmichael (1991).

FIGURE 5 Histograms of analyzed forsterite mol% (Fo#) of olivine phenocryst in two Colima cone samples: **(a)** COL-1001B and **(b)** COL-1015. Also, plots of wt% NiO vs. Fo# for the most Mg-rich olivine analyses (highest 3 mol% Fo) in the same two samples: **(c)** COL-1001B and **(d)** COL-1015. A linear fit to the data is used to calculate wt% NiO in the most Fo-rich olivine analyzed in each sample for olivine-melt Ni-based thermometer (Pu et al., 2017).

FIGURE 6 Back-scattered electron (BSE) images of diffusion-limited growth (dendritic and hopper) textures in olivine phenocrysts from **(a, b, c)** COL-1015 and **(d)** COL-1001.

FIGURE 7. (a) Plot of calculated temperatures from anhydrous Mg-thermometer of Pu et al. (2017), based on analyzed $D_{Mg}^{ol/liq}$ from experimental run products (Table 3), versus experimental temperatures. Solid line is 1:1 relationship; dashed lines are ±50°C. Top-down experiments (this study) are shown in blue whereas the bottom-up experiments (this study) are shown in red. Also shown (gray) are three hydrous experiments from Moore and Carmichael (1998), with the Ni contents in glass in the run products analyzed by Pu et al. (2017). **(b)** same as (a) except calculated temperatures are from anhydrous Ni-thermometer of Pu et al. (2017); **(c)** same as (a) except calculated temperatures are from the H_2O-corrected Mg-thermometer of Putirka et al. (2007; their Eq. 4). Also shown (open symbols) are results for 32 hydrous, near-liquidus (≤5% olivine) phase-equilibrium experiments from the literature (see text for details, no Ni contents in these experiments were not reported to calculate T_{Ni} for Fig. 7b). The collective data from this figure show that the Ni-thermometer of Pu et al. (2017), which does not include any correction for H_2O, recovers experimental temperatures equally well as the H_2O-corrected Mg-thermometer of Putirka et al. (2007).

FIGURE 8. Plot of calculated temperature using the H_2O-corrected Mg-thermometer of Putirka et al. (2007) vs. calculated temperature using the Ni-thermometer of Pu et al. (2017) for all 15 experiments in this study (black circles) plus three experiments from Moore and Carmichael (1998) (gray circles). Also shown are calculated temperatures for five natural samples from the Mexican arc (Table 6). When there is no H_2O correction, the Mg-thermometer of Putirka et al. (2007) gives temperatures (open squares) that deviate strongly from temperatures calculated with the Ni-thermometer of Pu et al. (2017). However, when the maximum analyzed H_2O contents in olivine-hosted melt inclusions in these five samples (Table 6) are used to obtain H_2O-corrected temperatures (green squares) from the Mg-thermometer of Putirka et al. (2007), the results match (within error) those from the Ni-thermometer of Pu et al. (2017). Solid line is 1:1 relationship; dashed lines are ±50°C.

FIGURE 9 (a) T_{expt} - T_{calc} vs P(GPa) plot for the application of the Mg- and Ni- thermometers from Pu et al. (2017; Eq. 1, Table 1) on all anhydrous experiments from Matzen et al. (2013; 2017). The blue line that shows excellent consistency with the residuals from the Mg-thermometer is the Herzberg and O'Hara (2002) pressure correction model (Eq. 2). The black line is the pressure correction model that was fit for T_{Ni} residual from Pu et al. (2017; Eq. 1, Table 1) at 1-3 GPa, shown on this plot. **(b)** T_{expt} - T_{calc} vs P(GPa) plot for the application of Matzen et al (2017) model on all anhydrous experiments from Matzen et al. (2013; 2017). The average residual is -20±33˚C.

FIGURE 10. (a) Plot of T_{calc} - T_{expt} vs. T_{expt} for the 123 1-bar experiments compiled by Pu et al. (2017; Eq.1), the six 1-bar experiments from this study and the four 1-bar experiments from Matzen et al. (2017) for the T_{Ni} model from Pu et al. (2017); **(b)** same as (a) but for the T_{Mg} model from Pu et al. (2017); **(c)** same as (a) but for the Matzen et al. (2017) model: $\ln(D_{Ni}^{ol/liq}) = \ln(D_{Mg}^{ol/liq}) + 4505/T(K) - 2.075$.

This is the peer-reviewed, final accepted version for American Mineralogist, published by the Mineralogical Society of America.
The published version is subject to change. Cite as Authors (Year) Title. American Mineralogist, in press.
DOI: https://doi.org/10.2138/am-2020-7014. http://www.minsocam.org/

Table 1 Fitted parameters and statistics for calibration of Eq.1 for i = Ni, Mg (from Pu et al., 2017).

	T_{Ni}	T_{Mg}
	fitted value ± 1σ	
a	-4.32 ± 0.33	-4.74 ± 0.20
b	9416 ± 296	6701 ± 182
c	-0.71 ± 0.13	-1.12 ± 0.08
d	0.53 ± 0.24	-1.08 ± 0.15
e	0.35 ± 0.11	0.64 ± 0.07
	statistics	
SEE	29	26
R^2	0.96	0.96

1184
1185

This is the peer-reviewed, final accepted version for American Mineralogist, published by the Mineralogical Society of America.
The published version is subject to change. Cite as Authors (Year) Title. American Mineralogist, in press.
DOI: https://doi.org/10.2138/am-2020-7014. http://www.minsocam.org/

Table 2 Composition of the natural sample UR-46 (Ownby et al., 2011), the synthesized glass at 1250˚C, and the glass and olivine in the near-liquidus 1-bar experiment at 1240˚C in this study.

sample name	UR-46*	UR46Ni glass**	1240˚C melt ***	1240˚C olivine (Fo89.8)***
SiO_2 (wt%)	52.2	51.6(4)	52.7(5)	41.0(2)
TiO_2 (wt%)	0.80	0.78 (2)	0.82(2)	-
Al_2O_3 (wt%)	16.7	17.3(1)	17.8(1)	0.08(2)
FeO^T (wt%)	7.39	7.49(13)	6.49(19)	9.79(19)
MnO (wt%)	0.13	0.14(2)	0.14(2)	0.18(3)
MgO (wt%)	9.38	9.55(8)	8.93(21)	48.4(2)
CaO (wt%)	9.26	8.64(6)	8.94(12)	0.43(4)
Na_2O (wt%)	3.37	3.47(6)	3.45(7)	-
K_2O (wt%)	0.56	0.59(3)	0.60(3)	-
P_2O_5 (wt%)	0.14	0.37(3)	0.14(2)	-
Ni (ppm)	231	353(19)	-	1320(237)
Total	100.1	100.5	99.51	100.6

All reported oxide wt% values are after normalized to 100%.
*from Ownby et al. (2011)
** UR-46 glass synthesized with added NiO powder.
***The 1240˚C experiment was conducted at NNO. The melt Fe^{2+}/Fe^{3+} ratio was calculated using Kress and Carmichael (1991). $^{Fe\text{-}Mg}_{oliv/liq}K_D$ is 0.35.

This is the peer-reviewed, final accepted version for American Mineralogist, published by the Mineralogical Society of America.
The published version is subject to change. Cite as Authors (Year) Title. American Mineralogist, in press.
DOI: https://doi.org/10.2138/am-2020-7014. http://www.minsocam.org/

Table 3a Conditions and run products of 1-bar experiments in gas mixing furnace

Expt #	22	22-1	23-2	20-1	21-1	21
Trajectory	Bottom-Up	Bottom-Up	Bottom-Up	Top-Down	Top-Down	Top-Down
T_1 (˚C)	-	-	-	1275	1275	1275
t_1 (h)	-	-	-	2	2	2
T_{final} (˚C)	1225	1225	1225	1225	1200	1200
t_{final} (h)	12	24	24	24	24	8
Phases proportion in wt%	glass (98.3); olivine (1.7)	glass (98.7); olivine (1.3)	glass (99.7); olivine (0.3)	glass (99.1); olivine (0.9)	glass (95.8); olivine (4.2)	glass (98.2); olivine (1.8)
% FeO change	1%	1%	1%	1%	1%	0%
% NiO change	-1%	-20%	-3%	-15%	-5%	6%
D_{Ni} (±1s.d.)	11.5 (2.2)	11.2 (0.7)	10.9 (0.6)	10.4 (1.3)	13.3 (1.6)	10.9 (1.7)
D_{Mg}(±1s.d.)	4.12 (0.06)	4.07 (0.07)	4.08 (0.09)	4.04 (0.02)	4.57 (0.07)	4.16 (0.10)
∆NNO	0	0	+2	0	0	0
Melt viscosity (log Pa-s)*	2.97	2.94	2.93	2.94	3.25	3.19
****Fe^{3+}/Fe^{T}**	0.20	0.20	0.38	0.20	0.20	0.20
$^{Fe\text{-}Mg}K_D$**	0.35 (.01)	0.36 (.01)	0.34 (.01)	0.36 (<.01)	0.35 (.01)	0.37 (.01)

1189

Table 3b Conditions and run products of 0.5 GPa anhydrous experiments in piston cylinder

Expt #	PC33	PC35
Trajectory	Bottom-Up	Bottom-Up
T_1 (˚C)	-	-
t_1 (h)	-	-
T_{final}^{***} (˚C)	1192	1192
t_{final} (h)	48	29.5
Phases proportion by weight	glass (79); olivine (8); plagioclase (13)	glass (98); olivine (2)
% FeO change	8%	11%
% NiO change	-6%	-26%
D_{Ni} (±1 s.d.)	11.9 (1.9)	13.7 (1.2)
D_{Mg}(±1 s.d.)	4.67 (0.08)	4.38 (0.07)
H_2O (wt%) by FTIR	0.20	0.20
Melt viscosity (log Pa-s)*	2.68	2.72
Fe-Mg K_D****	0.35 (.01)	-
Fe^{3+}/Fe^{T}	0.26	-

This is the peer-reviewed, final accepted version for American Mineralogist, published by the Mineralogical Society of America.
The published version is subject to change. Cite as Authors (Year) Title. American Mineralogist, in press.
DOI: https://doi.org/10.2138/am-2020-7014. http://www.minsocam.org/

1190

Table 3c Conditions and run products of 0.5 GPa hydrous experiments in piston cylinder

Expt#	PC10	PC12	PC13	PC14	PC37	PC17	PC36
Trajectory	Bottom-Up	Bottom-Up	Top-Down	Top-Down	Top-Down	Top-Down	Top-Down
T_1 (˚C)	-	-	1200	1225	1225	1225	1225
t_1 (h)	-	-	4	1	1	1	1
T_{final}* (˚C)**	1137	1127	1127	1127	1112	1102	1102
t_{final} (h)	12	12	12	8	8	8	8
Phases proportion by weight	glass (95.9); olivine (4.2)	glass (95.5); olivine (4.5)	glass (95.5); olivine (4.5); opx (<0.1)	glass (96.5); olivine (3.5)	glass (99.1); olivine (0.9)	glass (96.7); olivine (3.3)	glass (97.9); olivine (2.1)
% FeO change	-1%	4%	5%	7%	9%	2%	1%
% NiO change	1%	33%	-26%	1%	-15%	28%	3%
D_{Ni} (±1 s.d.)	17.2 (2.3)	15.5 (1.5)	17.6 (1.4)	17.8 (2.6)	15.3 (1.3)	15.7 (1.7)	15.0 (1.3)
D_{Mg} (±1 s.d.)	4.89 (0.05)	4.94 (0.06)	4.79 (0.07)	4.63 (0.09)	4.04 (0.04)	4.57 (0.04)	4.46 (0.08)
H_2O (wt%) by FTIR	4.0	4.3	2.0	2.8	3.0	3.0	3.6
Melt viscosity (log Pa-s)*	1.03	1.05	1.73	1.37	1.37	1.54	1.31
$_{Fe\text{-}Mg}K_D$****	0.32 (.01)	-	-	0.33 (.01)	-	-	-
Fe^{3+}/Fe^T	0.48	-	-	0.31	-	--	-

*Melt viscosity calculated with Hui and Zhang (2007)
**K_D calculated using Kress and Carmichael (1991) model to calculate melt Fe^{3+}/Fe^T at experimental T and fO_2
***Experimental temperature corrected for a +12˚C thermal gradient between PC thermocouple and the center of the capsule (see Appendix A for details)
****K_D calculated using Fe^{3+}/Fe^T measured by microXANES technique and glass composition analyzed by Electron Microprobe (see Table 4)

1191
1192

This is the peer-reviewed, final accepted version for American Mineralogist, published by the Mineralogical Society of America.
The published version is subject to change. Cite as Authors (Year) Title. American Mineralogist, in press.
DOI: https://doi.org/10.2138/am-2020-7014. http://www.minsocam.org/

Table 4 Olivine and melt compositions in all Ni partitioning experiments

Expt#	T (˚C)	Phase	n	SiO_2	TiO_2	Al_2O_3	FeO^T	MnO	MgO	CaO	Na_2O	K_2O	P_2O_5	NiO	Cr_2O_3	Total*	Ni**	H_2O (FTIR)	olivine Fo#	Total***
1-bar																				
22	1225	gl	28	52.29(26)	0.76(1)	17.53(16)	7.47(9)	0.13(1)	9.00(28)	8.72(6)	3.34(8)	0.63(3)	0.13(5)			100.51	283(26)	-		
		ol	6	41.25(22)		0.09(2)	10.98(20)	0.17(3)	46.70(38)	0.22(3)				0.52(9)	0.06(1)	99.99	-	-	88.4(3)	
22-1	1225	gl	26	52.14(31)	0.77(2)	17.38(17)	7.53(10)	0.13(2)	9.09(10)	8.79(11)	3.40(6)	0.63(4)	0.13(3)			100.33	241 (8)	-		
		ol	19	41.31(40)		0.07(2)	11.13(10)	0.16(1)	46.55(46)	0.23(2)				0.43(2)	0.06(1)	99.94	-	-	88.2(2)	
23-2	1225	gl	22	52.09(46)	0.77(2)	17.17(14)	7.53(12)	0.13(2)	9.45(14)	8.68(7)	3.42(6)	0.63(3)	0.13(4)			100.27	331 (12)			
		ol	13	41.48(43)		0.07(1)	8.29(10)	0.16(1)	48.83(81)	0.20(2)				0.58(2)	0.04(1)	99.65			91.3(2)	
20-1	1225	gl	24	52.01(21)	0.76(1)	17.48(19)	7.55(4)	0.13(1)	9.28(13)	8.74(6)	3.30(9)	0.62(3)	0.13(3)			100.38	271 (16)	-		
		ol	7	40.47(15)		0.09(4)	11.02(10)	0.17(3)	46.90(21)	0.23(3)				0.45(5)	0.06(0)	99.39	-	-	88.4(1)	
21-1	1200	gl	31	52.48(36)	0.78(1)	18.06(24)	7.35(10)	0.13(1)	8.01(20)	8.93(8)	3.46(8)	0.65(3)	0.15(4)			100.51	201 (13)	-		
		ol	43	40.80(31)		0.07(2)	11.92(18)	0.18(3)	46.37(38)	0.21(1)				0.43(4)	0.06(1)	100.05	-	-	87.4(2)	
21	1200	gl	25	52.11(42)	0.77(2)	17.62(26)	7.42(17)	0.13(2)	8.91(26)	8.77(11)	3.47(10)	0.65(3)	0.15(4)			100.18	270 (28)	-		
		ol	10	40.83(36)		0.08(2)	11.47(23)	0.17(2)	46.71(40)	0.22(2)				0.47(6)	0.05(2)	100.01	-	-	87.9(3)	
anhydrous high pressure																				
PC33	1192	gl	20	51.18(43)	0.90(9)	17.34(29)	8.80(13)	0.14(1)	7.66(10)	9.07(14)	4.06(9)	0.69(5)	0.17(4)			98.55	174(15)	0.2		98.8
		ol	35	40.50(14)		0.07(2)	13.06(34)	0.19(3)	44.67(40)	0.23(2)				0.33(5)	0.03(1)	99.10	-	-	85.9(4)	
PC35	1192	gl	18	51.56(32)	0.78(3)	17.40(16)	8.24(11)	0.13(1)	8.53(12)	8.55(10)	3.82(9)	0.63(3)	0.35(4)			100.22	197 (8)	0.2		100.2
		ol	12	41.43(37)		0.10(5)	10.38(21)	0.18(3)	47.72(32)	0.21(1)				0.44(3)	0.03(1)	100.50			89.1(2)	
hydrous																				
PC10	1137	gl	9	52.49(95)	0.79(1)	17.84(16)	7.37(5)	0.15(4)	7.84(10)	9.09(7)	3.48(7)	0.63(2)	0.32(4)			95.81	191 (19)	4.0		99.8
		ol	13	41.80(47)		0.05(1)	7.72(14)	0.17(3)	49.52(34)	0.18(0.01)				0.54(5)	0.02(1)	100.01	-	-	92.0(2)	
PC12	1127	gl	10	52.59(42)	0.78(1)	17.74(27)	7.72(7)	0.13(2)	7.67(27)	9.21(11)	3.24(14)	0.60(3)	0.32(3)			95.00	255 (23)	4.3		99.3
		ol	8	41.19(44)		0.06(2)	8.72(8)	0.18(1)	48.24(37)	0.19(1)				0.64(3)	0.02(1)	99.24	-	-	90.8(1)	
PC13	1127	gl	36	52.77(38)	0.77(2)	17.60(22)	7.73(10)	0.14(3)	7.68(16)	8.85(7)	3.49(8)	0.64(2)	0.33(3)			97.67	134 (7)	2.0		99.7
		ol	33	41.30(20)		0.05(2)	11.03(28)	0.18(3)	46.59(21)	0.17(1)				0.38(2)	0.03(1)	99.71	-	-	88.3(3)	
PC14	1127	gl	36	51.96(41)	0.78(2)	17.82(23)	7.90(14)	0.13(4)	8.04(28)	8.84(9)	3.57(11)	0.61(2)	0.35(3)			96.72	204 (22)	2.8		99.5
		ol	28	41.06(40)		0.05(1)	10.58(28)	0.17(3)	47.54(52)	0.16(1)				0.59(6)	0.04(2)	100.18	-	-	88.9(3)	
PC37	1112	gl	15	51.95(37)	0.78(2)	16.82(22)	8.18(8)	0.13(1)	9.42(11)	8.29(8)	3.46(10)	0.61(4)	0.36(3)			96.81	294 (17)	3.0		99.8
		ol	8	41.44(29)		0.05(1)	8.89(16)	0.18(3)	48.02(22)	0.16(1)				0.72(4)	0.03(1)	99.49	-	-	90.6(2)	
PC17	1102	gl	29	52.68(26)	0.76(1)	17.78(20)	7.60(6)	0.13(2)	8.24(31)	8.65(12)	3.22(11)	0.59(2)	0.36(3)			96.63	278 (23)	3.0		99.6
		ol	36	42.21(35)		0.05(1)	8.41(19)	0.16(3)	48.16(28)	0.15(2)				0.71(5)	0.05(3)	99.90	-	-	91.1(2)	
PC36	1102	gl	28	52.17(55)	0.78(2)	17.47(27)	7.56(13)	0.14(2)	8.69(28)	8.98(20)	3.45(11)	0.63(5)	0.14(3)			94.97	264 (13)	3.6		98.6
		ol	46	41.50(33)		0.04(1)	7.99(17)	0.16(1)	49.92(36)	0.14(1)				0.65(5)	0.05(3)	100.46			91.8(2)	

*reported oxide contents are after normalization to anhydrous 100%; reported totals are original analyzed values. All analyzed by the Electron Microprobe except for Ni and H_2O in glass.

**in ppm; measured by Laser Ablation ICP-MS.

***sum of reported oxide total measured by the Electron Microprobe + measured H_2O by FTIR.

1193
1194
1195

This is the peer-reviewed, final accepted version for American Mineralogist, published by the Mineralogical Society of America.
The published version is subject to change. Cite as Authors (Year) Title. American Mineralogist, in press.
DOI: https://doi.org/10.2138/am-2020-7014. http://www.minsocam.org/

Table 5 Composition and temperature results of five natural samples from Mexican arc

sample name	JOR-44*	TAN-19*	APA-6*	COL-1001	COL-1015
		Whole-rock composition			
SiO_2 (wt%)	52.1	54.5	56.0	50.2	48.8
TiO_2 (wt%)	0.81	0.83	0.88	1.73	1.30
Al_2O_3 (wt%)	16.4	17.2	17.6	16.2	11.1
FeO^T (wt%)	7.45	6.82	6.69	9.58	7.43
MnO (wt%)	0.13	0.12	0.11	0.16	0.13
MgO (wt%)	9.29	7.92	6.35	6.16	13.18
CaO (wt%)	8.46	7.98	7.28	9.31	9.35
Na_2O (wt%)	3.47	3.68	3.84	3.30	2.20
K_2O (wt%)	0.74	0.77	1.07	2.15	3.94
P_2O_5 (wt%)	0.14	0.18	0.23	0.52	0.87
Ni (ppm)	261	156	120	58	363
Total	99.0	100.0	100.1	99.3	98.3
		Olivine composition			
max. Fo#	89.9	89.1	85.5	83.1	92.8
olivine NiO (wt%)	0.54	0.57	0.49	0.20**	0.59**
		Calculated temperature			
H_2O wt% (MI)***	5.7	4.6	3.9	6.2	6.7
T_{Mg} (°C) Pu'17	1240	1209	1183	1147	1327
T_{Ni} (°C) Pu'17	1177	1078	1075	1073	1199
T_{Mg} - T_{Ni} (°C) Pu'17	63	130	108	75	128
$T_{Mg\text{-}H2O\ corr}$ (°C) P'07****	1116	1106	1094	1045	1174
$T_{Mg\text{-}H2O\ corr}$ P'07 - T_{Ni} (°C) Pu'17	-61	28	19	-28	-25

* from Pu et al. (2017)

** from Figure 5

*** MI (melt inclusion) data from Johnson et al. (2009), Vigouroux et al. (2008), Maria and Luhr (2008)

**** Mg-thermometer with H_2O correction of Putirka et al. (2007)

This is the peer-reviewed, final accepted version for American Mineralogist, published by the Mineralogical Society of America.
The published version is subject to change. Cite as Authors (Year) Title. American Mineralogist, in press.
DOI: https://doi.org/10.2138/am-2020-7014. http://www.minsocam.org/

Table 6 Temperature results from Mg- and Ni- thermometers in Pu et al. (2017) & Putirka et al. (2007) for experiments in this study

Expt #	T_{expt} (±4/8 ˚C)*	H_2O (FTIR)	T_{Mg} (±26˚C) Pu'17**	T_{Mg} error (°C)***	T_{Mg} - T_{expt} (˚C)	T_{Ni} (±29 °C) Pu'17	T_{Ni} error (°C)***	T_{Ni} - T_{expt} (˚C)	$T_{Mg\text{-}H2O\ corr}$ (±29˚C) P'07	$T_{Mg\text{-}H2O\ corr}$ - T_{expt} ˚C
22	1225	-	1234	±5	9	1201	±46	-24	1222	-3
22-1	1225	-	1237	±6	12	1206	±15	-19	1226	1
23-2	1225	-	1235	±8	10	1210	±13	-15	1225	0
20-1	1225	-	1238	±3	13	1220	±30	-5	1227	2
21-1	1200	-	1207	±5	7	1174	±27	-26	1197	-3
21	1200	-	1232	±9	32	1213	±37	13	1221	21
PC33	1192	0.2	1198	±6	6	1191	±37	-1	1190	-2
PC35	1192	0.2	1218	±6	26	1160	±20	-32	1205	13
PC10	1137	4.0	1186	±3	49	1119	±28	-18	1104	-33
PC12	1127	4.3	1181	±4	54	1141	±21	14	1095	-32
PC13	1127	2.0	1195	±5	68	1117	±17	-10	1147	20
PC14	1127	2.8	1201	±7	74	1109	±30	-18	1138	11
PC37	1112	3.0	1239	±4	127	1134	±18	22	1166	54
PC17	1102	3.0	1205	±3	103	1137	±23	35	1135	33
PC36	1102	3.6	1209	±6	107	1141	±19	39	1130	28

*Error in experimental temperature is ±4 °C at 1-bar and ±8 °C at 0.5 GPa (PC experiments)
** results from the Mg-thermometer from Pu et al. (2017) is within 10˚C to the Mg-thermometer from Beattie (1993)
***T_{Mg} and T_{Ni} errors are propagated from uncertainty from the Mg and Ni analyses in olivine and glass (Table 4)

1199

This is the peer-reviewed, final accepted version for American Mineralogist, published by the Mineralogical Society of America.
The published version is subject to change. Cite as Authors (Year) Title. American Mineralogist, in press.
DOI: https://doi.org/10.2138/am-2020-7014. http://www.minsocam.org/

Figure 1

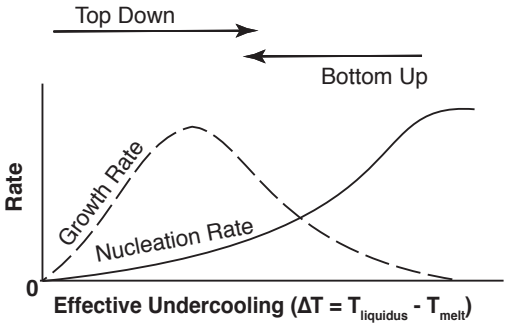

This is the peer-reviewed, final accepted version for American Mineralogist, published by the Mineralogical Society of America.
The published version is subject to change. Cite as Authors (Year) Title. American Mineralogist, in press.
DOI: https://doi.org/10.2138/am-2020-7014. http://www.minsocam.org/

Figure 2

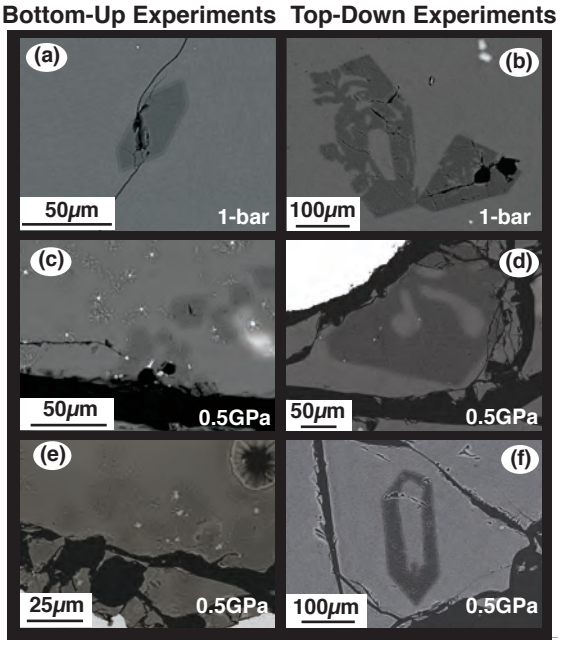

This is the peer-reviewed, final accepted version for American Mineralogist, published by the Mineralogical Society of America.
The published version is subject to change. Cite as Authors (Year) Title. American Mineralogist, in press.
DOI: https://doi.org/10.2138/am-2020-7014. http://www.minsocam.org/

Figure 3

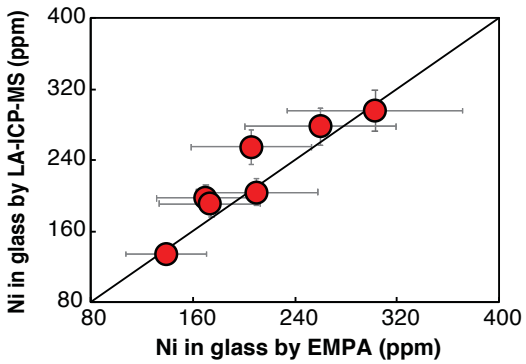

This is the peer-reviewed, final accepted version for American Mineralogist, published by the Mineralogical Society of America.
The published version is subject to change. Cite as Authors (Year) Title. American Mineralogist, in press.
DOI: https://doi.org/10.2138/am-2020-7014. http://www.minsocam.org/

Figure 4

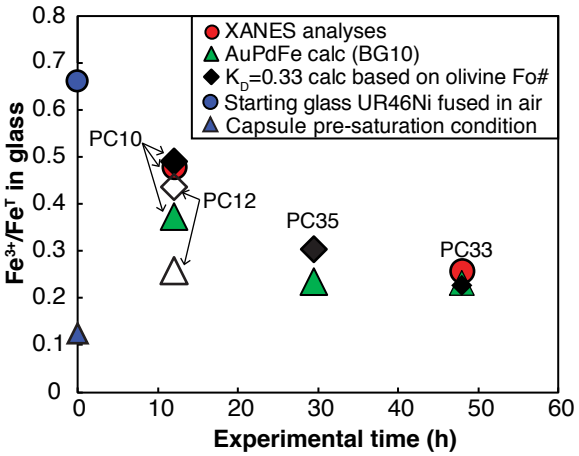

This is the peer-reviewed, final accepted version for American Mineralogist, published by the Mineralogical Society of America.
The published version is subject to change. Cite as Authors (Year) Title. American Mineralogist, in press.
DOI: https://doi.org/10.2138/am-2020-7014. http://www.minsocam.org/

Figure 5

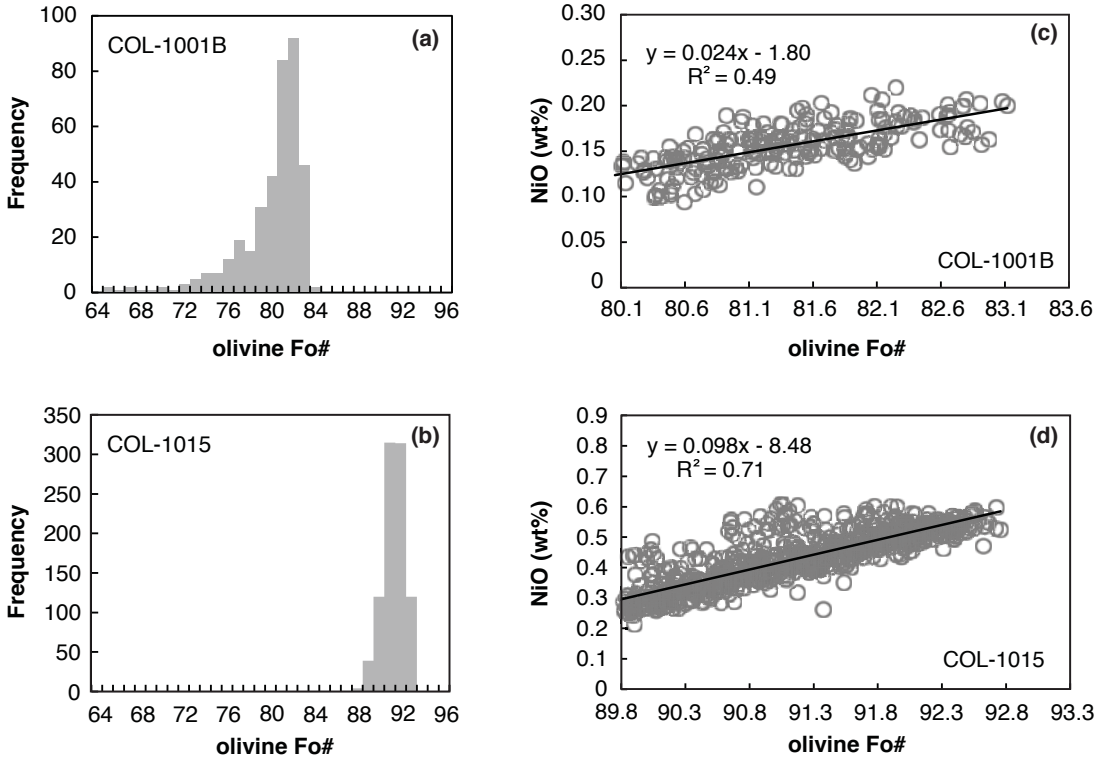

Figure 6

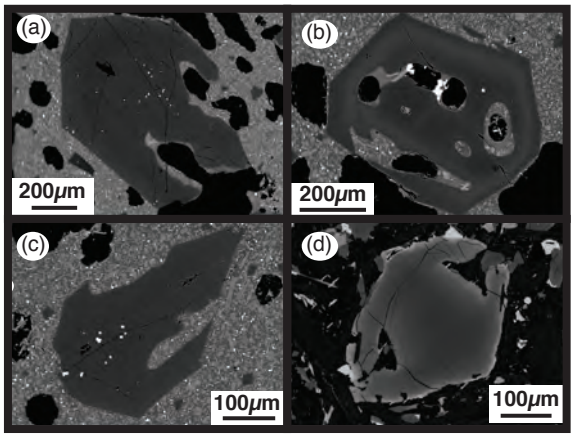

This is the peer-reviewed, final accepted version for American Mineralogist, published by the Mineralogical Society of America.
The published version is subject to change. Cite as Authors (Year) Title. American Mineralogist, in press.
DOI: https://doi.org/10.2138/am-2020-7014. http://www.minsocam.org/

Figure 7

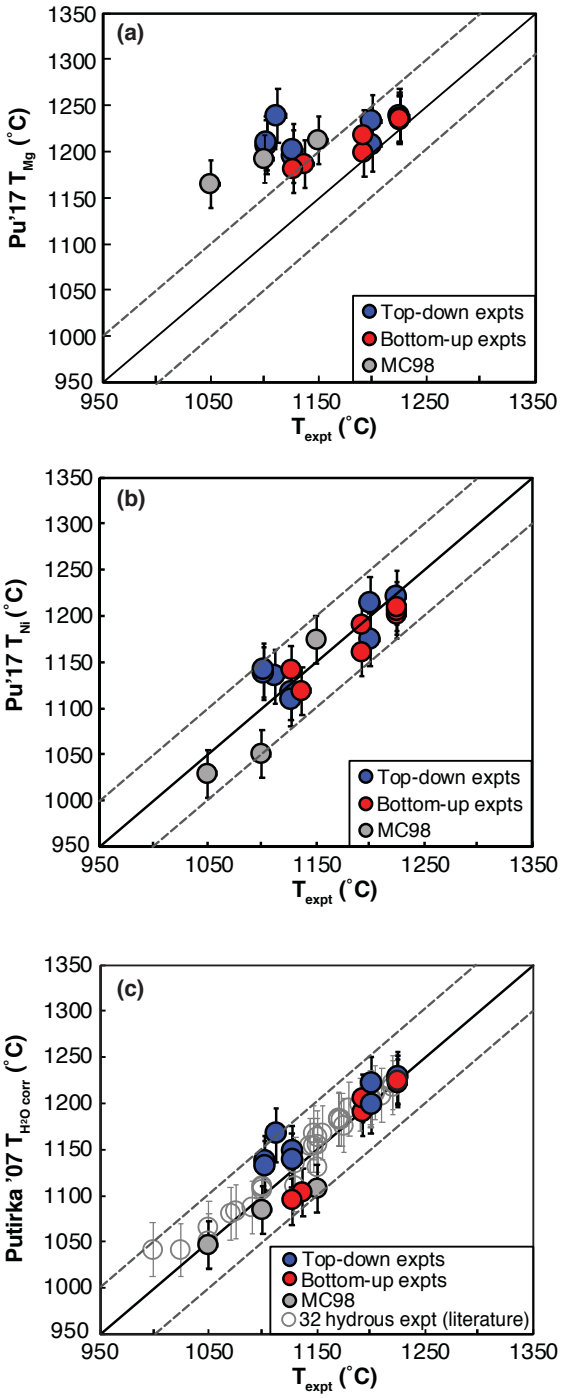

This is the peer-reviewed, final accepted version for American Mineralogist, published by the Mineralogical Society of America.
The published version is subject to change. Cite as Authors (Year) Title. American Mineralogist, in press.
DOI: https://doi.org/10.2138/am-2020-7014. http://www.minsocam.org/

Figure 8

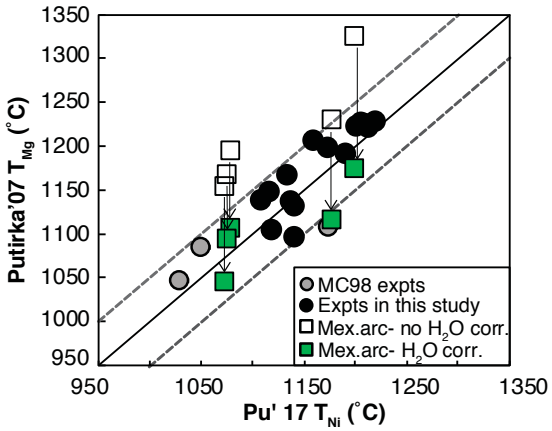

This is the peer-reviewed, final accepted version for American Mineralogist, published by the Mineralogical Society of America.
The published version is subject to change. Cite as Authors (Year) Title. American Mineralogist, in press.
DOI: https://doi.org/10.2138/am-2020-7014. http://www.minsocam.org/

Figure 9

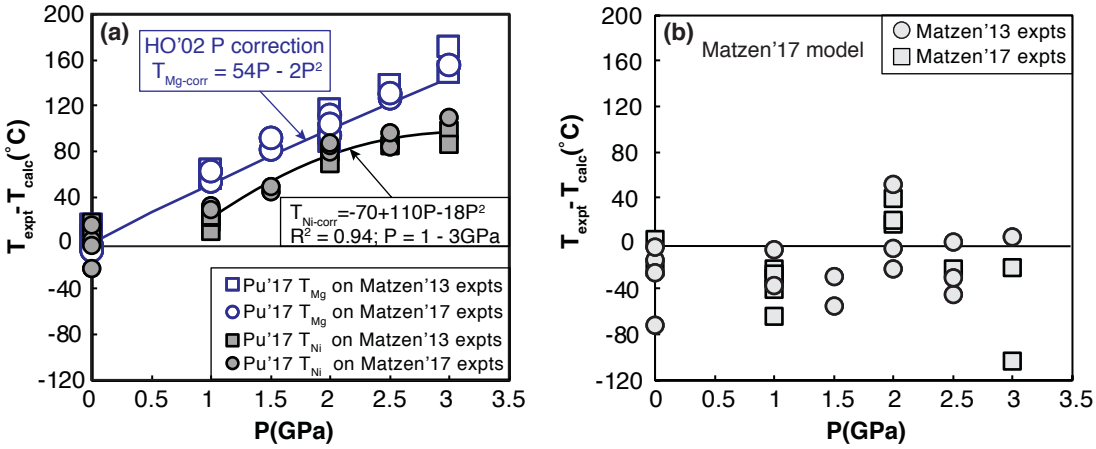

This is the peer-reviewed, final accepted version for American Mineralogist, published by the Mineralogical Society of America.
The published version is subject to change. Cite as Authors (Year) Title. American Mineralogist, in press.
DOI: https://doi.org/10.2138/am-2020-7014. http://www.minsocam.org/

Figure 10